Numerical Optimization of a Fully-Passive Flapping-Airfoil Turbine

Jean-Christophe Veilleux*, Guy Dumas

LMFN Laboratory, Département de génie mécanique, Université Laval
1065, avenue de la Médecine, Québec, Qc, Canada, G1V 0A6

Postprint, 2017 - Journal of Fluids and Structures
Published version available online at: https://doi.org/10.1016/j.jfluidstructs.2017.01.019

Abstract

This paper deals with an aeroelastic problem that consists into self-sustained, pitch-heave oscillations of an elastically-mounted airfoil. Such oscillations of an airfoil could be used in order to develop a novel, fully-passive hydrokinetic energy flow harvester that is relatively simple from a mechanical point of view. Indeed, the motion of such an airfoil emerges as a result of the fluid-structure interaction between the flow, the airfoil and its elastic supports, and is sustained through a net transfer of energy from the flow to the structure. In this numerical study, the *OpenFOAM-2.1.x* CFD toolbox is used for solving the aeroelastic problem. Through unsteady two-dimensional viscous simulations at a Reynolds number of 500,000, the fully-passive turbine is optimized and investigated to develop a better understanding of the physics at play. Following a gradient-like optimization of the turbine, two-dimensional efficiencies as high as 34% have been obtained, and two fundamental mechanisms have been found to be very beneficial for enhancing the performances of the turbine: the adequate synchronization between both degrees-of-freedom, and the nonsinusoidal shape of the pitching motion.

Keywords: CFD, fluid-structure interaction, unsteady aerodynamics, hydrokinetic turbines, oscillating foils

1. Introduction

The fluid-structure interaction of an airfoil with its surrounding fluid is of great interest in the design process of several devices and structures. It is well known that flutter is the result of a positive net exchange of energy from the fluid to the structure due to negative aerodynamic damping. Sometimes, one is not interested in having an accurate prediction of the total energy transfered to the solid body and only seeks an efficient way to determine whether the structure equilibrium is stable or not. Various successful analytical tools have been developed for this task. In other circumstances, an accurate prediction of this energy transfer is critical in order to avoid high-amplitude vibrations of a system. In such cases, the solution is to keep the relative transfer of energy from the fluid to the structure as low as possible when compared to the damping capacity of the apparatus. Conversely, structures undergoing flutter, such as airfoils, could be conceived as devices to harvest energy from an incoming fluid, thus transforming the flapping airfoil into some sort of novel turbine. Unlike the previous case, one would want the positive flux of energy from the fluid to the structure to be maximized, and, at the same time, make sure the machine could resist to these high-amplitude, flow-induced oscillations over the long terms.

Following the pioneering work of McKinney & DeLaurier (1980) in the field of flapping-wing turbines, significant research on the subject has been performed by several groups in the last decade with a general goal of optimizing the concept. The increasing amount of publications on this matter (see review paper of

*Corresponding author
Email address: jc.veilleux@caltech.edu (Jean-Christophe Veilleux)

Young et al. (2014)) is indicative of the rapidly growing interest towards the concept, which is justified by several advantages over the more conventional flow harvesters (see Guney & Kaygusuz (2010)). To state only a few of them, these bio-inspired turbines are not subject to the centrifugal stresses associated to the rotating blades found in most turbines. This makes the oscillating-foils devices structurally robust. Further, the oscillating foils sweep a rectangular flow window, which can be relatively wide and shallow. This is particularly interesting for the purpose of harvesting significant energy from rivers, especially those that are not very deep.

The promising potential of flapping foils as wind or hydrokinetic turbines has been confirmed both numerically (see Kinsey & Dumas (2006, 2008, 2012, 2014)) and experimentally (see Kinsey et al. (2011)) by the LMFN Laboratory (Laboratoire de Mécanique des Fluides Numérique) at Laval University. Several other groups also confirmed its potential, and the interested reader may refer to a recent review paper by Young et al. (2014) for an overview of the various concepts suggested and studied. Another recent review paper by Xiao & Zhu (2014) draws a clear portrait of the current state-of-the-art, and the main findings of several studies are gathered within this publication. In several of the concepts suggested, a rigid wing is mounted on a clever mechanical system in which the cyclic shape of the motion and the relation (phase lag) between the pitching, which is the angular motion, and the heaving, which is the translational motion, were enforced in such a way as to significantly increase the efficiency of the turbine, and the total energy it harvests from the flow (see Kinsey et al. (2011)). Among these systems, some involved a well-designed mechanical coupling between both motions, and this reduced the device to a single degree-of-freedom (DOF). Whether it has one or two DOFs, optimization of the energy harvester has typically been achieved through a direct implicit or explicit control on the functional shape, frequency and phase lag of the airfoil's motions in pitch and in heave. Energy harvesting efficiencies as high as 43% have been reported by Kinsey & Dumas (2014). Nevertheless, the mechanical components required to achieve this implicit or explicit control do add some mechanical complexity to the device, and this, in turns, may impair its *mechanical efficiency*, which should not be confused with the *energy harvesting efficiency*. A turbine concept not making use of such a mechanical coupling could therefore be greatly beneficial.

Recently, some research groups reported promising results concerning a simplified, semi-passive version of the flapping-foil flow harvester. In these semi-passive systems, the pitching motion of the foil is prescribed while the heave results naturally through the interaction of the foil with the flow and the supporting mechanism (see Shimizu et al. (2008); Zhu et al. (2009) and Zhu & Peng (2009)). Energy harvesting efficiencies as high as 25% have been reported following numerical studies, thus confirming the interesting potential of this simplified mechanism. An experimental study has also been conducted by Huxham et al. (2012) in a water tunnel, and efficiencies around 24% have been reported.

According to Zhu et al. (2009) and to Kinsey & Dumas (2008), flapping-airfoil devices essentially harvest the flow through the heaving motion. This means that the pitching motion produces or incurs only modest inputs/outputs of energy in the mean, which suggests the concept of a further simplified, fully-passive system (see Zhu (2011)). This idea that the pitching motion could be fully autonomous in an energetic sense has been experimentally (see Poirel et al. (2008)) and numerically (see Lapointe & Dumas (2011)) validated by observing self-sustained, pitching-only motion of a wing at transitional Reynolds numbers.

In a simplified fully-passive system, both the heaving and the pitching motions are entirely determined through the fluid-structure interaction between the foil, the flow and the elastic supports. Large-amplitude, self-sustained oscillations have been experimentally observed for such a system (see Dimitriadis & Li (2009); Mendes et al. (2011); Poirel & Mendes (2011) and Razak et al. (2011)). The relatively new idea of using a fully-passive system to harvest energy from a flow offers significant mechanical advantages over the preceding mechanisms at the cost of having no direct control over the motion of the foil. For a foil mounted on a rotational spring and a linear damper undergoing large-amplitude, cyclic oscillations, Peng & Zhu (2009) reported energy harvesting efficiencies up to 20%. Although the 2D numerical study was conducted at fairly low Reynolds number (Re = 1,000), it revealed the potential of this new kind of turbine, and further optimization of this passive system is probably at reach. However, as mentioned by the authors of the aforementioned paper, the response of the airfoil to the flow excitation might be significantly different for higher Reynolds numbers more representative of real turbine applications, and this remains to be investigated.

The optimization of the fully-passive, flapping airfoil must be achieved by adjusting parameters of the

apparatus having only an indirect effect on the motion of the foil, thus implying that a thorough understanding of the physics is critical. Note here that for the purpose of turbine applications, only cases for which limit-cycle oscillations (LCO) emerge are of interest. For such cases, the wing oscillates in a nonchaotic way with a single frequency for both DOFs, and the amplitudes of motion are relatively constant. This well-behaved motion of the airfoil is possible due to the nonlinearity of the aerodynamic forces, which is associated to the periodic dynamic stalling of the streamlined solid body (see Dowell et al. (2005)).

In this context of using a fully-passive, flapping airfoil as a wind or hydrokinetic turbine, Lapointe (2012), a former member of the authors' group, initiated a numerical study dealing with elastically-mounted, passive airfoils oscillating in transitional flows. The present investigation is an extension of this interesting work at higher, more practical Reynolds numbers. At this initial stage of the investigation, this paper aims to establish a proper FSI and optimization procedure, and to demonstrate the existence of local maxima of power extraction within the parametric space. A comprehensive parametric study is thus beyond the scope of the present work. Such study is ongoing and will be reported in a future paper together with the results of an experimental validation campaign. The present paper is thus divided as follows. The modeling and computational methodology is first introduced, followed by the presentation and the validation of the numerical solver. Then, an optimization of the turbine is presented along with a physical study of the mechanisms through which the performances are enhanced. Lastly, the main findings are summarized in a brief conclusion.

Before moving on to the next section, the reader should note that there remains some confusion in the literature on what a fully-passive, flapping-airfoil turbine really is. This is because some research groups consider that a device is fully-passive as soon as the motion is induced by the flow. Nevertheless, this is not strictly correct. This is because some devices make use of a mechanical linkage between both DOFs, thus imposing some constraints on the motion of the foils. However, actuators are not necessarily used in such cases, which means that the oscillations are entirely flow-induced. However, categorizing such devices as being fully-passive would certainly be misleading. In this work, the term *fully-passive* is exclusively reserved for devices where no actuators are present, and no mechanical linkage or coupling between the DOFs are used, thus for which both DOFs are freely responding unconstrained. The reader should refer to Kinsey & Dumas (2014) for a clarification on the terminology to be adopted.

2. Modeling and computational methodology

2.1. Aeroelastic modeling

In the aeroelastic problem of interest, the rigid, elastically-mounted airfoil is free to pitch around the z-axis and heave along the y-axis. This is clearly illustrated in Figure 1. The motion is not possible in any other direction, nor about any other axis. As schematically shown, the two-DOF system consists of a rigid airfoil which is mounted on a pivot about which the pitching motion (θ) is possible. Further, the pivot is mounted on a sliding mechanism (not shown), thus allowing the heaving motion (h).

Figure 1 also schematically depicts several key parameters of interest in the formulation of the aeroelastic problem. As previously suggested, the motion of the airfoil which is elastically-supported in a freestream flow and undergoing LCO may be indirectly controlled through a well-studied choice of all structural parameters. This is exactly what has to be achieved in the present study for the task of optimizing the device as a turbine. For clarity and convenience, all the parameters involved in the current aeroelastic problem are introduced in Table 1.

Figure 1 also introduces the main system of coordinates used throughout the study. It is defined such that it corresponds to a right-hand system with the x-axis rightward positive, and the y-axis upward positive. Further, gravity is assumed in the z-direction, which obviously excludes it from the dynamics of the 2D airfoil.

It is worth pointing out now that the heaving mass (m_h) and the pitching mass (m_p) of such a system do not need to be equal, and this must be taken into account within the equations of motion. One can convince oneself by considering Figure 2, which is the perfect example of an aeroelastic device where the mass of the sliding mechanism is *not* involved in the pitching motion of the airfoil. Last, it has been implied within

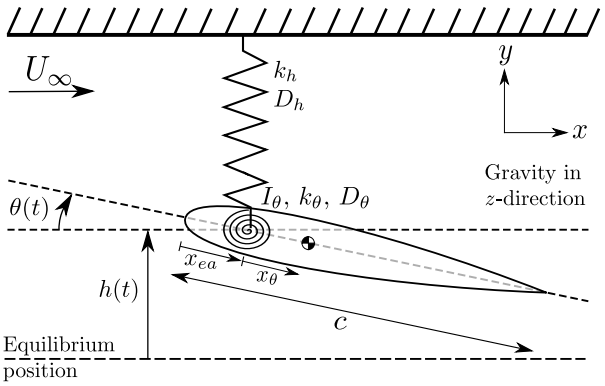

Figure 1: Simplified schematic of the symmetrical, rigid, elastically-mounted airfoil with symbolic representation of key parameters (not showing the sliding mechanism). Adapted from Lapointe & Dumas (2012).

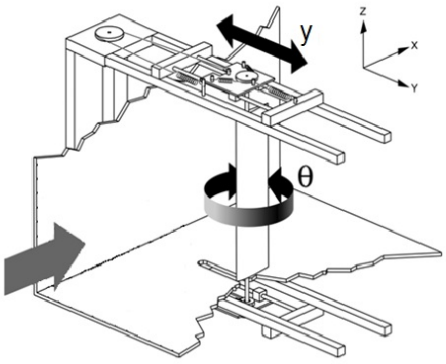

Figure 2: Schematic of the symmetrical, rigid, elastically-mounted airfoil used in the wind-tunnel experiment of the Royal Military College (RMC) in the transitional range of Reynolds numbers. Reproduced with permission from Poirel et al. (2006).

the previous enumeration of the flow and structural parameters that the effect of the electrical generator eventually connected to the device is here modeled as a viscous damper with a purely linear behavior. Such a hypothesis is commonly accepted, and more details are provided in Appendix A.

With this general picture of the fully-passive, flapping-airfoil turbine, the equations of motion can be derived in a fairly straightforward manner. The details of this derivation can be found in the thesis of Veilleux (2014). The final non-dimensional equations for the heave DOF and the pitch DOF are respectively:

$$\frac{C_\mathcal{L}}{2} = \underbrace{m_h^* \ddot{h}^*}_{\substack{\text{inertial}\\ \text{term}}} + \underbrace{S^* \left(\dot{\theta}^{*2} \sin\theta - \ddot{\theta}^* \cos\theta \right)}_{\substack{\text{inertial coupling}\\ \text{term}}} + \underbrace{k_h^* h^* + D_h^* \dot{h}^*}_{\substack{\text{structural}\\ \text{terms}}} , \tag{1}$$

$$\frac{C_M}{2} = \underbrace{I_\theta^* \ddot{\theta}^*}_{\substack{\text{inertial}\\ \text{term}}} - \underbrace{S^* \ddot{h}^* \cos\theta}_{\substack{\text{inertial coupling}\\ \text{term}}} + \underbrace{k_\theta^* \theta + D_\theta^* \dot{\theta}^*}_{\substack{\text{structural}\\ \text{terms}}} , \tag{2}$$

where the non-dimensional parameters are

$$C_\mathcal{L} = \frac{\mathcal{L}}{\frac{1}{2}\rho U_\infty^2 bc} , \quad C_M = \frac{M_{ea}}{\frac{1}{2}\rho U_\infty^2 bc^2} , \quad I_\theta^* = \frac{I_\theta}{\rho bc^4} , \quad k_\theta^* = \frac{k_\theta}{\rho U_\infty^2 bc^2} , \quad D_\theta^* = \frac{D_\theta}{\rho U_\infty bc^3} ,$$

$$k_h^* = \frac{k_h}{\rho U_\infty^2 b} , \quad D_h^* = \frac{D_h}{\rho U_\infty bc} , \quad m_h^* = \frac{m_h}{\rho bc^2} , \quad S^* = \frac{S}{\rho bc^3} , \quad h^* = \frac{h}{c} ,$$

$$\dot{h}^* = \frac{\dot{h}}{U_\infty} , \quad \ddot{h}^* = \frac{\ddot{h}c}{U_\infty^2} , \quad \dot{\theta}^* = \frac{\dot{\theta}c}{U_\infty} , \quad \ddot{\theta}^* = \frac{\ddot{\theta}c^2}{U_\infty^2} .$$

It is to be noted that the parameter ρ corresponds to the density of the fluid, and the so-called static imbalance ($S = m_p x_\theta$) has been used to reinforce the idea that $m_p x_\theta$ forms a single structural parameter.

Equations 1 and 2 constitute the two equations of motion of the fully-passive, flapping-airfoil turbine modeled in this study. In each, there is an aerodynamic force or moment with an inertial term, an inertial coupling term and two structural terms. The inertial coupling term explicitly couples the equations of motion when $S \neq 0$. It can be seen that no inertial coupling term is present when the elastic axis coincides with the center of mass of the pitching components ($S = 0$).

Table 1: List of all the parameters involved in the present aeroelastic problem.

Symbol	Parameter	Description
U_∞	freestream velocity	velocity of the undisturbed flow upstream of the airfoil
	airfoil's profile	the airfoil's profile is assumed rigid at all time
c	airfoil's chord length	distance between the leading edge and the trailing edge
m_p	pitching mass	mass of all components involved in the pitching motion
m_h	heaving mass	mass of all components involved in the heaving motion
I_θ	moment of inertia	airfoil's moment of inertia about the elastic axis (i.e., pitching axis)
x_{ea}	location of the elastic axis	distance between the elastic axis and the leading edge of the airfoil
x_θ	location of the center of mass	distance between the elastic axis and the center of mass (positive when the elastic axis is ahead of the center of mass)
k_h	heave stiffness coefficient	linear stiffness coefficient used to account for the restoring force of the linear spring
k_θ	pitch stiffness coefficient	linear stiffness coefficient used to account for the restoring moment of the torsional spring
D_h	heave damping coefficient	linear damping coefficient used to account for the dissipation of energy associated to the electrical generator connected to the oscillating airfoil and the structural damping in heave
D_θ	pitch damping coefficient	linear damping coefficient used to account for the dissipation of energy associated to structural damping in pitch
$\mathcal{L}$	aerodynamic lift	lift force generated by the flow on the airfoil (upward positive)
M_{ea}	aerodynamic moment	moment generated by the flow on the airfoil (clockwise positive)
$h(t)$	instantaneous heave position	vertical position of the elastic axis (upward positive), where the superscript $(\cdot)$ denotes its time derivative, thus the heaving velocity
$\theta(t)$	instantaneous pitch angle	angular position of the airfoil, i.e., geometric angle between the chord line and the freestream flow (clockwise positive), where the superscript $(\cdot)$ denotes its time derivative, thus the pitching velocity

There is another form of coupling between the above equations of motion. Contrary to the inertial coupling, the aerodynamic coupling is *always* present, whatever the choice of the structural parameters. Indeed, $\mathcal{L}$ and M_{ea} are always greatly linked together, and this implicitly[1] couples both equations of motion. As it may be observed, no other form of coupling is possible between the equations of motion, and this is in agreement with the modeled device: there is no mechanical linkage between the DOFs to control the phase lag between the motions, and there is no way to control explicitly the shape of any of the two motions.

Within the structural terms in the equations of motion, the assumed linear behavior of the restoring forces and moments, along with the damping forces and moments, may be viewed as a reasonable simplification over the physical reality. It is worth pointing out that even with this simplification in place, the two equations

[1]This coupling is referred to as implicit here because its presence is not obvious when looking at the equations of motion as written. Expressing the lift and aerodynamic moment as integrals of the wall stresses (pressure and shear) would make the link between the two more apparent. Conversely, the inertial coupling is explicit because it is obvious at first glance.

of motion contain a total of seven structural parameters, thus providing many ways to indirectly control the dynamics of the airfoil. The reader may appreciate the vast parametric space of this aeroelastic device, and, as a result, the richness of the physics embodied within the present problem. If nonlinearities were introduced within the model, this would add further dimensions and complexity to an already immense parametric space. This would certainly render this first study of the device much more challenging, perhaps even too convoluted to extract useful data.

It is useful to write an equation for the cycle-averaged power of such a device. As one might expect, once the airfoil has reached a permanent regime of motion, the inputs of power are exactly balanced by all outputs. Using such an equation will prove to be helpful at understanding better the fully-passive turbine. In order to obtain this equation, Eq. 1 and Eq. 2 must be multiplied by the heaving velocity and the pitching rate respectively. Once this is done, both equations can be summed and cycle-averaged. Of course, the cycle-averaged contribution of some terms is expected to be zero. This can be demonstrated by assuming a general cyclic motion for both DOFs and averaging each term over a complete cycle. The details of this can be found in the thesis of Veilleux (2014), but the final cycle-averaged equation for the power is:

$$\overline{C}_P \;=\; \overline{C}_{Py} \;+\; \overline{C}_{P\theta} \;=\; \overline{C}_{Py,damp} \;+\; \overline{C}_{P\theta,damp} \;, \tag{3}$$

where the different contributions are defined below in Table 2 and are cycle-averaged as

$$\overline{C}_P(\zeta) \;=\; \frac{1}{T}\int_0^T \frac{\zeta}{\frac{1}{2}\,\rho\, U_\infty^3\, bc}\; dt \;. \tag{4}$$

With this in hand, it is clear that over one complete cycle, in the mean, only the aerodynamics can provide some energy to the airfoil, while both damping terms provide the energy sinks. During each cycle when the airfoil is in a permanent regime, this equality must be satisfied. A more detailed and lengthy analysis, available in the thesis of Veilleux (2014), also reveals that there is a net power transfer between the two DOFs, which is given by:

$$\overline{C}_{P,tr} \;=\; \overline{C}_{Py} \;-\; \overline{C}_{Py,damp} = \; \overline{C}_{P\theta,damp} \;-\; \overline{C}_{P\theta} \;. \tag{5}$$

where

$$\overline{C}_{P,tr} \;=\; \overline{C}_P\left(S\left[\dot{\theta}^2\dot{y}\,\sin\theta - \ddot{\theta}\,\dot{y}\cos\theta\right]\right) \;=\; \overline{C}_P\left(S\left[\ddot{y}\,\dot{\theta}\cos\theta\right]\right) \tag{6}$$

This equation states two very important findings. First, and this is already known from Eq. 3, the inertial coupling term does not contribute, over one complete cycle, at providing or extracting some power to or from the airfoil: the cycle-averaged power calculated for the inertial coupling term coming from the equation of motion in heave exactly balances the contribution of the inertial coupling term coming from the equation of motion in pitch. Second, the inertial coupling terms provide a mean to transfer energy from one DOF to the other. However, it is not possible to predict ahead of time in what direction this will happen since this remains case dependent.

Table 2: Definition and description of the cycle-averaged power contributions.

Symbol	Definition	Description
$\overline{C}_{Py}$	$\overline{C}_P(\mathcal{L}\dot{y})$	cycle-averaged contribution from the aerodynamic lift
$\overline{C}_{P\theta}$	$\overline{C}_P(M_{ea}\dot{\theta})$	cycle-averaged contribution from the aerodynamic moment
$\overline{C}_{Py,damp}$	$\overline{C}_P(D_h\dot{y}^2)$	cycle-averaged contribution from the heave damping
$\overline{C}_{P\theta,damp}$	$\overline{C}_P(D_\theta\dot{\theta}^2)$	cycle-averaged contribution from the pitch damping

3. Fluid-structure solver

The fully-passive, flapping-airfoil problem is solved using *OpenFOAM-2.1.x*, a finite-volume, open-source CFD toolbox. For a complete description of the numerical methods readily available within the CFD toolbox, the reader is referred to the *OpenFOAM-2.1.x* official documentation (see OpenCFD (2012a,b)).

3.1. Equations of the flow

The equations of the flow, including the equations presented within the following subsection on the modeling of turbulence, are written using the indicial notation. The governing equations of the incompressible, viscous flow with constant and uniform properties are the continuity and the Navier-Stokes equations, which are respectively:

$$\frac{\partial u_i}{\partial x_i} \;=\; 0 \;, \tag{7}$$

$$\frac{\partial u_i}{\partial t} \;+\; u_j \frac{\partial u_i}{\partial x_j} \;=\; -\frac{1}{\rho_f}\frac{\partial p}{\partial x_i} \;+\; \nu \frac{\partial^2 u_i}{\partial x_j^2} \;, \tag{8}$$

where u_i are the velocity components, p is the pressure, x_i are the cartesian coordinates, ρ_f is the density of the fluid and ν is the kinematic viscosity.

In the current study, the PISO algorithm has been chosen in order to achieve the pressure-velocity coupling. In fact, both PISO and SIMPLE schemes (see Ferziger & Perić (2002)) have been tested, and the PISO algorithm has proved to be faster for the present application.

3.2. Turbulence modeling

In the present numerical study, the Reynolds number ($\mathrm{Re} = U_\infty c/\nu$) is set to a value of 500,000 unless otherwise noted. That being said, directly solving all scales of motion, including the turbulent ones, is strictly out of reach. Instead, the effect of turbulence has been taken into account through the Unsteady Reynolds-Averaged Navier-Stokes (URANS) approach due to its relative low cost.

Closure of the resulting system of equations is achieved using the Spalart-Allmaras, one-equation turbulence model originally presented by Spalart & Allmaras (1994), except that no trip term is present. This corresponds to what is known as the fully-turbulent mode of the Spalart-Allmaras model. As demonstrated by Rumsey & Spalart (2008), this turbulence model intends to be used for fully-turbulent, high Reynolds number flows, and should never be used to predict the laminar to turbulent transition. This is one main reason why the fully-turbulent mode is preferred by most users of this model.

Previous work in the authors' research group at the LMFN on pitch-heave oscillations of an airfoil, such as Julien et al. (2007) and Lapointe & Dumas (2012), have validated the use of the Spalart-Allmaras turbulence model for flapping-airfoil problems. The authors came to the conclusion that although this model does not always provide excellent quantitative agreement with experimental data, the qualitative results and the trends are typically fairly good and reliable. It is recalled that this study is primarily concerned with the general trends and engineering predictions of the physical responses. Further, a good agreement between the URANS simulations and the experimental results has been obtained for the kinematically-constrained, flapping-airfoil device developed by the LMFN at Laval University (see Kinsey & Dumas (2012)). Although this provides a good level of confidence in the present the approach used to model the effect of turbulence, further validation is nonetheless presented in the next section.

3.3. Dynamic mesh and boundary/initial conditions

In the current implementation, the pitching and heaving airfoil problem is conveniently solved in a non-inertial frame of reference. The translational, heaving motion of the airfoil is taken into account via a proper volume, momentum source term effective over the entire calculation domain (100 chords $\times$ 100 chords), along with unsteady boundary conditions on the velocity at all inlets. The purpose of these boundary conditions is simply to add a time-varying y-component of velocity on the frontiers of the calculation domain. This

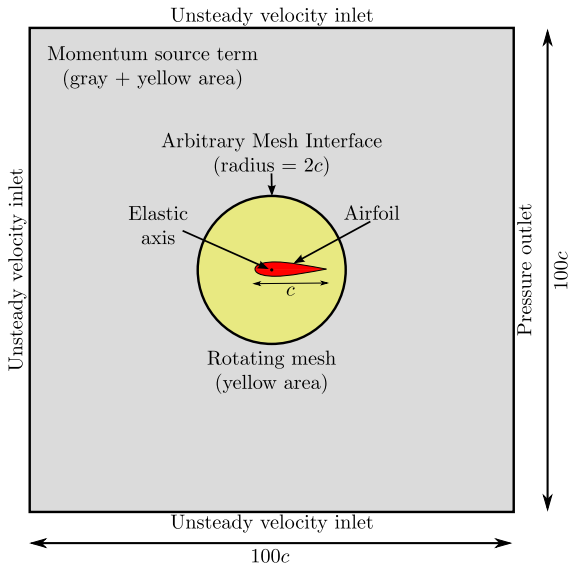

Figure 3: Configuration of the computational domain (not shown to scale) with its dimensions, the boundary condition types and the main features for solving the aeroelastic problem in a heaving reference frame.

component of velocity, in order to account for the heaving velocity of the airfoil, must be equal to the opposite of the heaving velocity ($-\dot{h}$). Although the pitching motion of the airfoil could be accounted for by a radially-non-uniform source term, using simple moving-body and moving-grid capabilities was the preferred approach for the present work. As shown in Figure 3, the central, circular portion of the mesh, which has a radius of 2 chords, is free to rotate about an axis passing through the circle's center. In fact, this rotating mesh is adjusted so that its center coincides with the elastic axis of the airfoil, and the instantaneous orientation of this dynamic portion of the mesh is simply set equal to the airfoil's angular position (θ). At the interface between the static and the dynamic portions of the mesh, an interpolation scheme is required due to the obvious non-conformity of the grids. This is achieved with the native *OpenFOAM* Arbitrary Mesh Interface algorithm (see Farrell & Maddison (2011)).

This idea of solving the problem in the heaving frame of reference and using dynamic meshes for the pitching motion has been proposed and validated in the past by Kinsey & Dumas (2008) and Lapointe & Dumas (2011). The accuracy of the method has also been confirmed in the present investigation through the general validation of the solver. The main advantage of this technique is surely that it avoids remeshing and deforming meshes, which can be penalizing in terms of accuracy and quite demanding in terms of computational cost.

Figure 3 also shows the boundary conditions used on the computational domain. The boundary conditions are detailed in Table 3, where the derivative of a given parameter ϕ in a direction perpendicular to a boundary is written as $\partial\phi/\partial n$, and the value of the flow velocity ($\mathbf{u}$) is given in the form of a vector.

Concerning the initial conditions of the numerical problem, each simulation is initialized with uniform pressure and velocity fields throughout the domain. The initial value of the pressure field is set to zero, while the value of the velocity field corresponds to the superposition of the freestream velocity (U_∞) along the x-axis, and the opposite of the initial heaving velocity ($-\dot{h}_i$) along the y-axis. A uniform value of the turbulent viscosity field is also used throughout the domain. The prescribed value is the same as the one prescribed at the inlets (see Figure 3 and Table 3). Last, an initial heaving velocity ($\dot{h}_i$) and/or an initial pitching rate ($\dot{\theta}_i$) of the foil can be imposed at the beginning of the calculation. These initial velocities may model an eventual external perturbation with which the airfoil might be disturbed from its equilibrium position. Such a perturbation is not always required for the LCO to develop, but it has been found that an adequate choice of these initial velocities can greatly help to shorten the duration of the transient regime, which in turns shortens the total computational time. As a rule of thumb, a heaving initial perturbation

Table 3: Boundary conditions used for solving the aeroelastic problem of a fully-passive, flapping-airfoil turbine in a heaving reference frame using *OpenFOAM-2.1.x*. Refer to Figure 3 for the location of each boundary in the calculation domain.

Boundary	Parameter	Type	Value
Unsteady velocity inlet	$\mathbf{u}$	Dirichlet	$\mathbf{u} = (U_\infty, -\dot{h}, 0)$
	p	Neumann	$\frac{\partial p}{\partial n} = 0$
	ν_t	Dirichlet	$\nu_t/\nu = 1$
Pressure outlet	$\mathbf{u}$	Neumann	$\frac{\partial \mathbf{u}}{\partial n} = 0$
	p	Dirichlet	$p = 0$
	ν_t	Neumann	$\frac{\partial \nu_t}{\partial n} = 0$
Airfoil's surface	$\mathbf{u}$	Dirichlet	$\mathbf{u} = (0, 0, 0)$
	p	Neumann	$\frac{\partial p}{\partial n} = 0$
	ν_t	Dirichlet	$\nu_t = 0$

$\dot{h}_i = 0.1U_\infty$ combined with the absence of an initial perturbation in pitch is generally an adequate initial setting.

3.4. Fluid-structure coupling

Fluid-structure interaction (FSI) is a multiphysics problem that involves a *two-way* interaction between the fluid and the structure. Indeed, the motion of the structure very often arises from the fluctuating forces generated by the fluid on the structure. In turns, the motion of the structure typically alters the flow pattern close to the structure (see He et al. (2012) and Yang et al. (2008)), which of course affects the forces. The strength of this dual interaction, which is often referred to as the FSI strength, is certainly variable and dependent upon various parameters. Howbeit, some situations where this two-way coupling between the equations of the fluid flow and the equations of the structure is not negligible are frequently encountered in practice, and this is certainly the case of airfoils undergoing LCO as a result of stall flutter. Various approaches can be used to couple the equations of the flow with the equations of the structure, and the reader who might be interested in having more details on the various coupling schemes is referred to Olivier (2014), Tezduyar et al. (2006) and Tian (2014).

In the present study, a staggered, explicit coupling scheme has been chosen due to its lower numerical cost. In this approach, no subiterations are carried out within a numerical time step. A typical example of such coupling scheme is shown in Figure 4. The numbers above the lines indicate the sequence of events, and the schematic depicts clearly that a single iteration is performed, thus leading immediately to the next-step solution for each solver (i.e., no intermediate solution is present). This, of course, is achieved at the cost of being susceptible to the well-known instability of such an explicit fluid-structure coupling scheme (often referred to as the added mass instability in theoretical analyses involving potential flow solvers; see Causin et al. (2005); Degroote et al. (2008); Förster et al. (2007) and He et al. (2012)). For fully-passive, flapping-airfoil wind turbines, this is certainly not an issue as a result of the low fluid's density, thus leading to a fairly weak fluid-structure interaction. However, for a hydrokinetic turbine, this numerical stability criterion may restrict a little, but not critically, the size of the parametric space that can be investigated with the implemented tools. Indeed, hydrokinetic turbines are typically conceived with a lower density ratio than what is found in wind turbines, and the strength of the FSI may be significantly more important. In the future, a more robust solver which is able to handle lower density ratios could be implemented. This robust

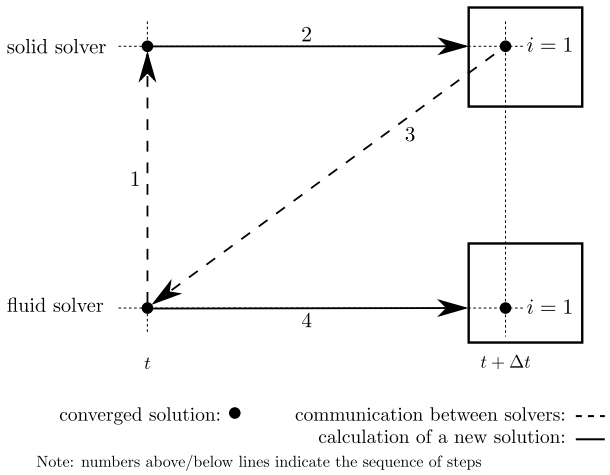

Figure 4: A typical explicit coupling scheme between the solid and the fluid solvers in a staggered, fluid-structure interaction CFD solver.

solver, for example, could use a sub-stepping strategy or under-relaxation (see Tian (2014), Bhardwaj & Mittal (2012) and Tian et al. (2014).

3.5. Numerical schemes and solvers

To complete the description of the numerical methodology used to solve the aeroelastic problem, the various numerical schemes and solvers used to solve the equations of the flow should at least be mentioned. The transient terms are discretized using a second-order backward implicit scheme, while the convective terms are treated with a second-order scheme based on a linear upwind interpolation. Finally, the diffusive terms are discretized using a second-order scheme based on a linear interpolation, and an explicit non-orthogonal-limited surface-normal gradient scheme is also used. Furthermore, the linear equations solver is a generalized geometric-algebraic multigrid (GAMG) method for both the pressure and momentum equations, while a smooth solver using Gauss-Seidel method is used for the transport equation of ν_t.

For the task of solving the equations of motion of the airfoil (Eqs. 1 and 2), the system of two differential equations of degree two is decomposed into a system of four differential equations of degree one. The resulting system of equations is then solved using a 4^{th} order Runge-Kutta method (see Fortin (2001)) readily available within *OpenFOAM-2.1.x*.

4. Validation of the FSI solver

Validation of the numerical methodology is achieved in two complementary ways. The first validation test is conducted using some experimental results for a fully-passive, flapping airfoil investigated at the RMC in Kingston, Ontario, Canada. The second validation test involves the well-documented aeroelastic problem of an oscillating cylinder.

4.1. Flapping airfoil

A research group at the Royal Military College (RMC) in Ontario conducted an experimental study on an airfoil that was elastically-mounted in both pitch and heave in a fashion that is very similar to the aeroelastic device of this paper. The experimental study, which is described in details in the papers of Mendes et al. (2011) and Poirel & Mendes (2011), and summarized by Veilleux (2014), was conducted in the transitional range of Reynolds number (Re = [50,000 to 120,000]). Although this remains far from the range of Reynolds numbers representative of a turbine application, these results turn out to be very useful for the

Table 4: Constant parameters in the experiment of the fully-passive, elastically-mounted airfoil conducted at the Royal Military College (RMC) (see Mendes et al. (2011); Poirel (2012); Poirel et al. (2008) and Poirel & Mendes (2011)).

Parameter	Value
c	0.156 m
x_{ea}	0.186 c
x_θ	0.095 c
I_θ	0.00135 kg·m^2
k_θ	0.3 N·m/rad
D_θ	0.002 N·m·s/rad
m_h	2.5 kg
S	0.0114 kg· m

purpose of validating the fluid-structure interaction (FSI) solver. Indeed, a validation has been carried out through two-dimensional numerical simulations aiming to replicate the experiment.

The set of structural parameters reported in Table 4 has been used throughout this validation. Further, both the low heave stiffness case ($k_h = 800\ N/m$) and the large heave stiffness case ($k_h = 1484\ N/m$) from the experiment have been replicated, but only the later is reported here for brevity. The complete results can be found in the thesis of Veilleux (2014). As the reader will soon realize, this test case is not only used in order to assess the physical validity of the numerical results: it is also used to demonstrate the independence of the present results from the numerics.

4.1.1. Baseline numerical values

The baseline numerical parameters presented here are those used for predicting the motion of the airfoil in the transitional range of Reynolds numbers, as well as for the case at Re = 500,000. In all simulations of this paper, a time step providing a minimum of 3,000 steps per period of oscillation (T) and a minimum of 200 steps per convective time unit (c/U_∞) is used:

$$\Delta t \ = \ \min\left\{ \frac{1}{3000\ f} \ , \ \frac{c}{200\ U_\infty} \right\} \ , \tag{9}$$

where f is the observed frequency of oscillation. Further, a baseline convergence criterion of 1×10^{-5} is enforced on the normalized pressure residuals, while a criterion of 1×10^{-6} is used for both the momentum and the turbulent quantities.

The 2D computational grid used is shown in Figure 5, and it is in agreement with the general description of the computational domain shown in Figure 3. The grid is built with approximately 65,000 cells with close to 450 points on the airfoil. The first cell thickness is set in order to respect $y^+ \approx 1$ on the airfoil's surface for all simulations. It must be clear that the mesh used for the simulations in the transitional range of Reynolds numbers is the same for all velocities of the freesteam flow, which means that the first cell thickness has been chosen according to the most restrictive case considered (i.e., Re = 120,000). Further, the 2D grid used for the numerical study at Re = 500,000 is very similar to this one: only the wall-normal resolution has been slightly refined in order to again respect a value of $y^+ \approx 1$.

Concerning the turbulent viscosity ratio, a value of $\nu_t/\nu = 1$ is used at all inlets of the computational domain. This yields negligible turbulent diffusivity at a station immediately upstream of the airfoil. Some simulations have been carried out with a ratio of ν_t/ν greater and lower by one and two orders of magnitude (i.e., ratio of ν_t/ν of 0.01, 0.1, 10 and 100), and no significant variations have been observed on the numerical results. Furthermore, a value of $\nu_t/\nu = 1$ is consistent with the recommended value for the Spalart-Allmaras turbulence model when used in the fully turbulent mode (see Spalart (2000) and Spalart & Rumsey (2007)).

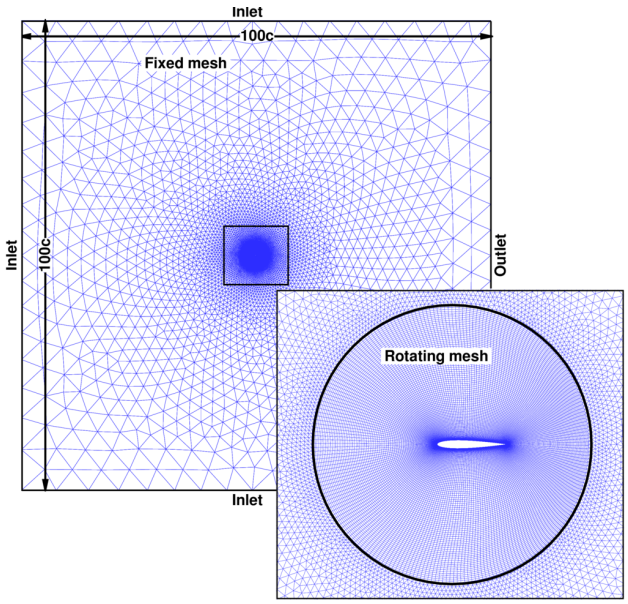

Figure 5: Main features of the computational grid used for the numerical simulations in the transitional range of Reynolds numbers, as well as for those at Re = 500,000.

All simulations are initialized with a perturbed airfoil unless otherwise noted. This is achieved here by specifying an initial heaving velocity ($\dot{h}_i$). The parameter $\dot{h}_i$ is set to approximately 5-10% of U_∞. After trying several initial perturbations, it has been found that such a value of $\dot{h}_i$ typically shortens the duration of the transient regime, and it has been verified that the terminal LCO regime is not dependent upon this initial perturbation unless an excessively large perturbation is used. When such an excessively large perturbation is provided, the airfoil simply flips over (i.e., $\theta > 180°$), and this rapidly has disastrous consequences on the numerical solution.

4.1.2. Results' independence

The independence of the numerical results from the time step size has been demonstrated by varying the time step from the baseline criterion provided by Eq. 9. Table 5 shows the effect of varying the time step, which is quantified by computing the RMS value over three complete cycles of oscillations for the lift coefficient ($C_\mathcal{L}$), the aerodynamic moment coefficient about the elastic axis (C_{Mea}), the drag coefficient ($C_\mathcal{D}$), and the motion in both pitch (θ) and heave (h). The relative variations shown are in percents, and they have been computed by taking the most refined case as the reference. The most refined time step provides 26,000 steps per period of oscillation and 2,400 steps per convective time unit. Using the baseline requirement instead of the fine time step did not affect noticeably the results. Variations of less than 0.2% are observed on both motions, and variations of 0.75% or less are observed on the aerodynamic forces and moments. Conversely, a coarser time step providing 500 steps per period and 50 steps per convective time unit has also been investigated, and variations of less than 0.4% are observed on both amplitudes of motion, but the differences are in the range of 2% to 3% for the aerodynamic forces and moments. These results confirm that the baseline requirement provided by Eq. 9 is adequate.

Concerning the numerical convergence criteria used on the physical quantities, a refinement and a coarsening of one order of magnitude from the baseline values did not significantly affect any of the parameters recorded. The maximum differences on $C_\mathcal{L}$, C_{Mea} and $C_\mathcal{D}$ have been found to remain below 0.01%, which is certainly a very negligible difference. The same observations hold true for both motions. As a result, it could be justified to use the coarser criteria, but using the coarser criteria does not provide much gain in computational time. For this reason, it remains safer to use the baseline values.

Table 5: Relative effect of the time step with respect to the most refined simulation results on the lift coefficient ($C_{\mathcal{L}}$), the aerodynamic moment coefficient (C_{Mea}) and the drag coefficient ($C_{\mathcal{D}}$), along with its effect on the motion in both pitch (θ) and heave (h).

Time step	$C_{\mathcal{L}}$ (%)	C_{Mea} (%)	$C_{\mathcal{D}}$ (%)	θ (%)	h (%)
Coarse (500 steps/cycle)	2.63	2.20	3.12	0.40	0.18
Baseline (3,000 steps/cycle)	0.42	0.59	0.72	0.16	0.05
Fine (26,000 steps/cycle)	—	—	—	—	—

Table 6: Relative effect of the grid resolution on the lift coefficient ($C_{\mathcal{L}}$), the aerodynamic moment coefficient (C_{Mea}) and the drag coefficient ($C_{\mathcal{D}}$), along with its effect on the motion in both pitch (θ) and heave (h).

Mesh	$C_{\mathcal{L}}$ (%)	C_{Mea} (%)	$C_{\mathcal{D}}$ (%)	θ (%)	h (%)
Coarse (30,000 cells)	0.52	1.37	1.62	0.88	0.17
Baseline (65,000 cells)	0.13	0.97	1.38	0.67	0.18
Fine (120,000 cells)	—	—	—	—	—

Mesh refinements in the rotating portion of the grid have been considered both in the streamwise and the wall-normal directions. The validation has been achieved with a run on a coarse grid of approximately 30,000 cells with approximately 250 points on the airfoil, and with a run on a refined grid of approximately 120,000 cells with 650 points on the airfoil. The results are shown in Table 6, where the same quantities as before are used to quantify the effect of the mesh resolution. Once again, the relative differences, in percents, are calculated using the fine grid as a reference. As shown, the variations on $C_{\mathcal{L}}$, C_{Mea} and $C_{\mathcal{D}}$ are in the range of 1.6% and below for both the coarse and the baseline grid, and the differences on θ and h remain well below 1%. It should be noted that the parameter most influenced by the grid resolution, namely the drag coefficient, is not involved in the equations of motion of the fully-passive, flapping airfoil. Therefore, these results confirm that using the baseline grid is sufficient and adequate for the current purpose.

At last, because all computations have been performed on multiple processors in parallel, the results of a serial computation have been compared to those of a parallel computation achieved on eight cores. All quantities checked matched nearly perfectly, thus indicating the adequate parallelization of the tools used to solve the present aeroelastic problem.

4.1.3. Comparison with experimental results

Because the structural damping coefficient (D_h) for the experimental setup of the RMC is a function of the instantaneous heaving amplitude, a hypothesis has been made concerning the value of the heave damping coefficient: the damping ratio (ξ_h) in heave is considered to be constant and equal to the asymptotic value for a large amplitude of motion in heave. The complete analysis, which is shown in Veilleux (2014), yields a damping coefficient of $D_h = 2\ Ns/m$.

Using this with the aforementioned parameters of Table 4, several numerical simulations have been performed for the range of freestream velocities (U_∞) investigated in the wind-tunnel experiment of the RMC, namely between 4.68 m/s, which corresponds to Re = 50,000, and 11.23 m/s, which corresponds to Re = 120,000. However, it should be mentioned that experimental results are not available throughout this complete range of freestream flow velocities for the large heave stiffness case. This is because the amplitude of motion of the flapping airfoil became large enough to fear that it would impair its structural integrity.

Experimental and CFD results are gathered in Figures 6 and 7, where the reduced frequency ($f^* = fc/U_\infty$), the normalized heaving amplitude (h_0/c) and the pitching amplitude (θ_0) are shown for various Reynolds numbers. The decoupled reduced natural frequencies for both the pitch ($f_{N,p}\, c/U_\infty$) and the heave

($f_{N,h}\, c/U_\infty$) degrees-of-freedom are also plotted, where:

$$f_{N,p} \;=\; \frac{1}{2\pi}\sqrt{\frac{k_\theta}{I_\theta}}\;, \tag{10}$$

$$f_{N,h} \;=\; \frac{1}{2\pi}\sqrt{\frac{k_h}{m_h}}\;. \tag{11}$$

As it can be observed in Figure 6, a single frequency of oscillation emerges for this two-degree-of-freedom device (i.e., the frequencies in pitch and in heave are the same). It can be seen that an excellent match is obtained between the experimentally measured frequencies and the numerically predicted frequencies for the limited range of Reynolds numbers covered by the experiment. For both the experimental and the CFD values, the apparatus oscillates at a frequency nearly identical to the calculated decoupled natural frequency in heave ($f_{N,h}$). This indicates that aerodynamic stiffening in heave is not significant in this specific regime of oscillation. However, the aerodynamic stiffening is significant on the rotational motion of the airfoil. Outside of the experimental range, the predicted frequencies still agree fairly well with the decoupled natural frequency in heave, but there is no way to tell if this is in agreement with the experiment. Furthermore, the values predicted without using any turbulence model, which are labeled as laminar, are almost identical to those predicted using the Spalart-Allmaras URANS model. This is not unexpected at these moderate Reynolds numbers.

Figure 7 shows that the experimentally measured amplitudes of motion compare well with those predicted through the FSI solver over the limited experimental range of Reynolds numbers. Nevertheless, as previously mentioned, the experiment on the large heave stiffness case has been stopped at a lower freestream flow velocity due to the rapid growth of the amplitudes of motion. That being said, the predicted values indeed show that both amplitudes of motion keep growing beyond the maximum wind-tunnel velocity for which results are published. This appears to be in qualitative agreement with the observations performed at the RMC.

Concerning the laminar results shown in Figure 7, some error bars are shown as a way to quantify the amount of fluctuations within the predicted amplitudes of motion from one cycle to the other[2]. The average amplitude is therefore displayed with error bars extending up to the maximum and the minimum amplitudes recorded. These laminar simulations predict amplitudes that are slightly lower or equal to those predicted with the Spalart-Allmaras turbulence model. It must be noted that the differences between the predictions of both series increase as the Reynolds number grows.

Unfortunately, the experimental uncertainties over the results, as much as the uncertainties over the structural parameters of the device, have not been addressed in the work of the RMC. Nevertheless, the good agreement with the experimentally measured values is a first confirmation of the validity of the FSI solver used in this numerical study. Furthermore, the numerical results obtained with and without the modeling of turbulence are definitely in the same range of values, and the trends are the same.

The comparison between the experiment and the numerical simulations for the low heave stiffness case also shows a good agreement. For this case (not presented here), simulations using the SST $k-\omega$ turbulence model have also been performed, and they match very well the results obtained with the Spalart-Allmaras turbulence model (see Veilleux (2014)).

4.2. Vortex induced vibrations of a cylinder

In order to further validate the FSI solver, a relatively simple and well-documented aeroelastic problem is used. It consists of a rigid, two-dimensional cylinder which is elastically mounted in a freestream flow. The cylinder only has one degree-of-freedom: it is free to oscillate transversally to the flow (i.e., along the y-axis). The configuration of the benchmark is schematically depicted in Figure 8.

[2]Indeed, stable LCO are not quite obtained through laminar simulations. Instead, a modulation of the amplitudes is observed.

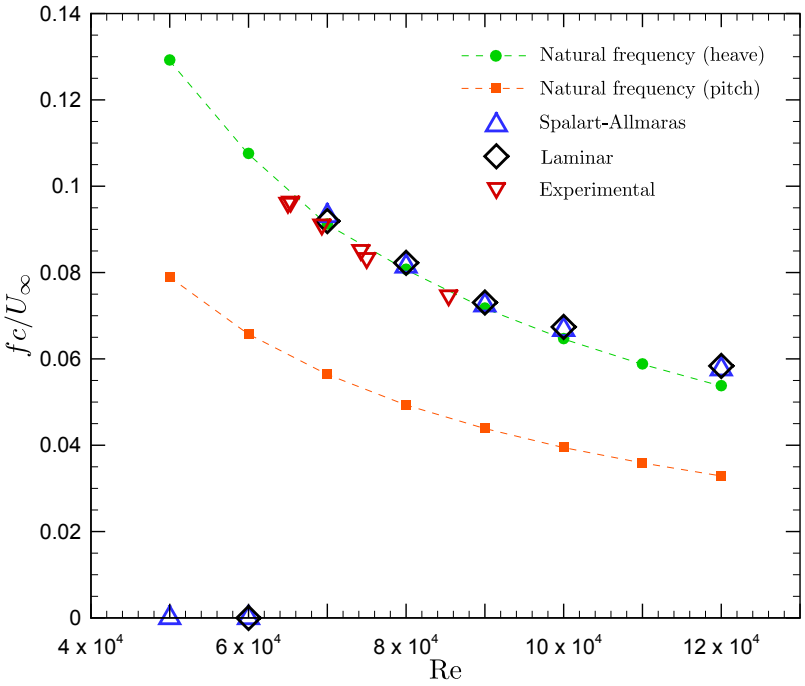

Figure 6: Comparison of the numerically predicted reduced frequencies with the experimentally measured reduced frequencies and with the calculated decoupled natural structural frequencies for the large heave stiffness case ($k_h = 1484\ N/m$). Experimental values from Poirel (2012) and Poirel & Mendes (2011).

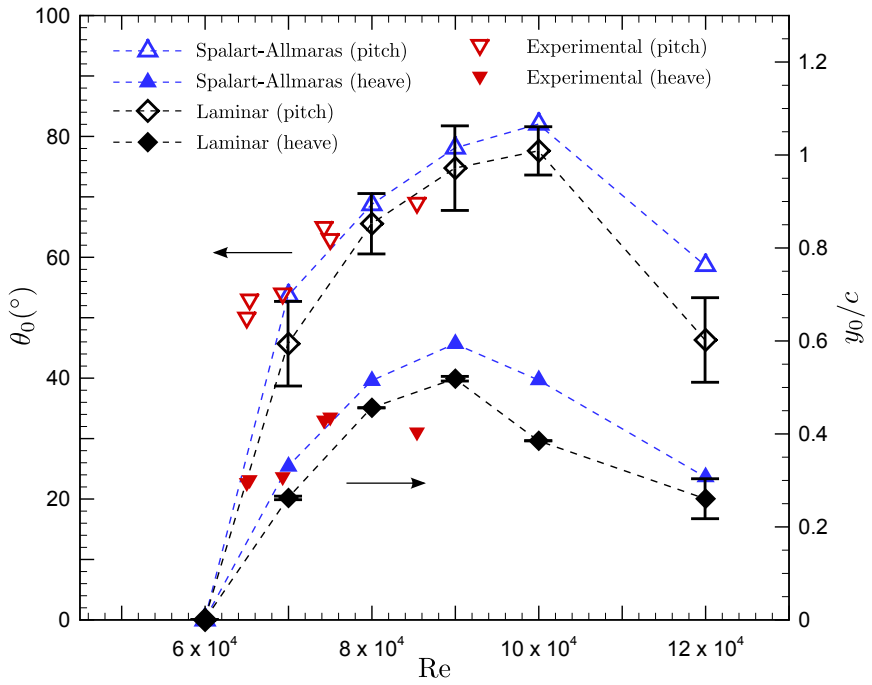

Figure 7: Comparison of the numerically predicted amplitudes of motion in both pitch and heave with the experimentally measured amplitudes of motion for the large heave stiffness case ($k_h = 1484\ N/m$). Error bars on the laminar results show the amount of fluctuations within the amplitude of motion from one cycle to the other. Experimental values from Poirel (2012) and Poirel & Mendes (2011).

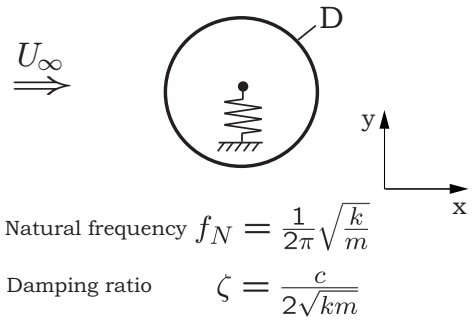

Figure 8: Schematic of the elastically-mounted cylinder which is free to oscillate transversally to the freestream flow. Reproduced from Morissette (2009).

The physical explanation to the self-sustained and self-induced oscillations of the cylinder is relatively simple: they are due to the alternating vortex shedding behind the cylinder. Because vortex shedding is the key element here, the phenomenon has been given the name of vortex induced vibrations (VIV), a phenomenon which is very well documented in the literature (see Williamson & Govardhan (2004) for a comprehensive discussion on this matter). The motion of such a cylinder is governed by the following equation:

$$F = m\ddot{y} + c\dot{y} + ky \ , \tag{12}$$

where F is the fluctuating vertical force, m is the mass of the cylinder, c is the structural damping coefficient, and k is the spring stiffness coefficient. All these parameters are given per unit depth of the cylinder. Further, y, $\dot{y}$ and $\ddot{y}$ are respectively the vertical position, the velocity and the acceleration of the cylinder's center of mass, which is located at the center of the cylinder. As the reader may already have noticed, Eq. 12 is very similar to the equation of motion in heave of the fully-passive, flapping airfoil (Eq. 1). The only difference is the absence of the inertial coupling term in the case of the oscillating cylinder.

4.2.1. Validation using numerical studies

The results obtained with the current numerical solver are compared with the results of three numerical studies from the literature. The first numerical study is from Yang et al. (2008), where the laminar results have been obtained using a strong coupling scheme between the equations of the incompressible flow and the cylinder's equation of motion. The second numerical study is from Leontini et al. (2006), and the results have been obtained through a spectral-element method which was coupled to the harmonical equation of the cylinder. The third and last numerical study is from Morissette (2009), a former student from the authors' research group. His numerical results have been obtained using both an in-house lagrangian vortex method, and the commercial CFD software *Fluent 6.3*. As the reader may note, these three numerical studies cover a wide spectrum of different numerical methods to solve the same aeroeslastic problem. Despite this variability, the numerical results of all studies are in very good agreement.

The set of non-dimensional parameters is shown in Table 7 using the following definitions:

$$m^* = \frac{\rho_s}{\rho_f} \ , \tag{13}$$

$$\xi = \frac{c}{2\sqrt{km}} \ , \tag{14}$$

$$U^* = \frac{U_\infty}{f_N D} \ , \tag{15}$$

Table 7: Set of non-dimensional parameters used in the reference numerical studies and the present one.

Physical parameter	Symbol	Value
Reynolds number	Re	200
Non-dimensional mass	m^*	10
Damping ratio	ξ	0.01
Non-dimensional velocity	U^*	4.5

Table 8: Results from the numerical studies of the one-degree-of-freedom elastically-mounted cylinder performed by Yang et al. (2008); Leontini et al. (2006) and Morissette (2009), along with the results of the present study.

Results	A^*_{max}	$C_{y,max}$	f^*
Present	0.50	2.31	0.96
Morissette (2009) (vortex method)	0.49	2.22	0.95
Yang et al. (2008)	0.42	2.25	0.95
Leontini et al. (2006)	0.47	2.37	0.95

where ρ_s and ρ_f are respectively the density of the cylinder and the fluid, D is the diameter of the cylinder and $f_N = \sqrt{k/m}/2\pi$. The non-dimensional mass ($m^* = 10$) corresponds to a case where the strength of the FSI is moderate. Using such a value of m^* is challenging for the current FSI solver, and this particularly puts the present FSI coupling scheme to the test.

A simulation has been achieved with the same parameters as those shown in Table 7. The calculations on the elastically-mounted cylinder have been performed on a 2D grid that has approximately 55,000 cells. Further, a non-dimensional time step ($\Delta t U_\infty/D$) of 0.005 has been used. The rest of the numerical methodology is exactly the same as the one presented earlier.

The normalized maximum amplitude of motion ($A^*_{max} = A_{max}/D$), the maximum force coefficient ($C_{y,max}$), and the reduced frequency of oscillation ($f^* = f/f_N$) of the past and the present numerical studies are shown in Table 8. A very good agreement is observed between the results from all studies, including the current one, and this provides good confidence in the FSI solver of this paper. Further, the displacement history (available in Veilleux (2014) agrees very well with that of Morissette (2009).

Another validation is achieved, this time using only the results of Leontini et al. (2006). To obtain the results of interest here, the same set of non-dimensional parameters as the one shown in Table 7 is used, except for one parameter: the non-dimensional velocity of the flow is now $U^* = 5.2$. The quantitative results of Leontini et al. (2006) and those of the present study are compared in Table 9. Again, an excellent agreement is obtained, and the displacement history of the cylinder agree very well.

Table 9: Results from the numerical study of the one-degree-of-freedom elastically-mounted cylinder performed by Leontini et al. (2006), along with the results of the present study for $U^* = 5.2$.

Results	A^*_{max}	$C_{y,max}$	f^*
Present	0.43	0.20	1.00
Leontini et al. (2006)	0.43	0.25	1.00

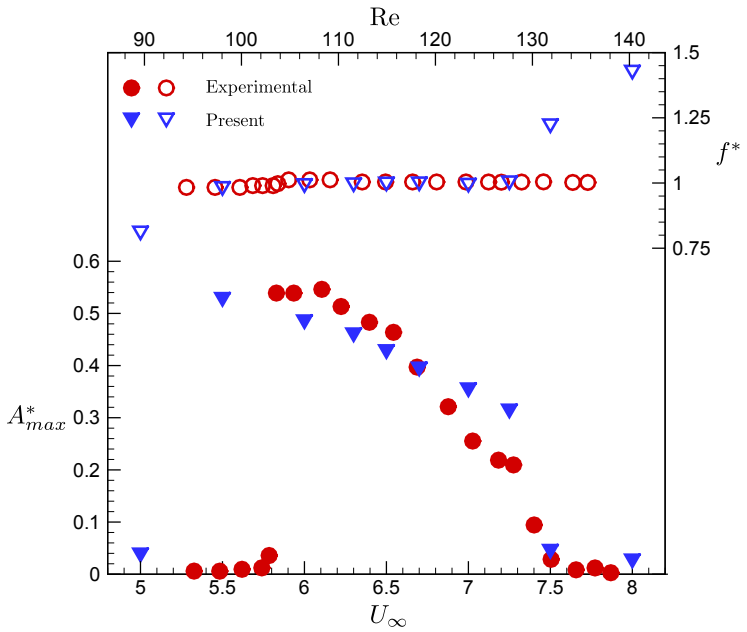

Figure 9: Normalized amplitude of motion (A^*_{max}) and reduced frequency of oscillations (f^*) for an elastically-mounted cylinder having a damping ratio (ξ) of 0.0012 and a non-dimensional mass (m^*) of 148.2. Experimental values from Anagnostopoulos & Bearman (1992).

4.2.2. Validation using an experimental study

To further assess the validity of the FSI solver, the numerical predictions obtained with the solver of this study are compared with the results of an experimental study. Anagnostopoulos & Bearman (1992) published one of the very few experimental studies in the laminar flow regime. In their water-channel experiment, the Reynolds number has been varied between 90 to 150, the damping ratio (ξ) was equal to 0.0012, and the non-dimensional mass (m^*) was equal to 148.2. This value of m^* corresponds to a FSI strength which is somewhat weak. Nevertheless, this test case offers a great validation opportunity, and the physics is somewhat different from the previous cases.

A comparison of the normalized maximum amplitude of motion of the cylinder (A^*_{max}) and the reduced frequency of oscillation (f^*) is shown in Figure 9 over the complete range of flow velocities covered within the experiment. A good match is observed between the experiment and the present numerical simulations over most of the velocity range. A slight discrepancy is noted in the vicinity of $U^* = 5.5$. From the experimental data, it is observed that the amplitude of motion quickly drops between $U^* = 5.5$ and $U^* = 6.0$. However, the FSI solver predicts that this happens between $U^* = 5$ and $U^* = 5.5$. Another slight discrepancy is observed, this time concerning the frequency. The results from the experiment show that the cylinder oscillates at a frequency very close to the natural frequency for all velocities of the flow. However, the FSI solver predicts a larger frequency of oscillation for $U^* > 7.5$, and a lower frequency for $U^* = 5$. It is believed that these slight discrepancies could be explained by the presence of dry friction in the experimental setup, but this remains to be confirmed.

Globally, these results confirm that the 2D predictions made with the present FSI solver are in the same range as the experimentally measured values. Further, the predicted trends are generally in good agreement with the experiment. This again provides a confirmation that the FSI solver of this thesis can be used with confidence for the sake of studying the aeroelastic problem of a fully-passive, flapping-airfoil turbine.

4.3. Assessment of the FSI scheme's limitations

Williamson & Govardhan (2004) gathered and discussed the results of several studies dealing with the

Table 10: Results of the computations performed with a constant value of $\Lambda = 0.11$ while the strength of the fluid-structure interaction is increased (i.e., m^* is decreased). The label N/A stands for *not available*, and is used whenever the solver is unable to provide results due to a numerical instability of the present explicit coupling scheme.

m^*	ξ	A^*_{max}	C_{ymax}	f^*
10	0.010	0.43	0.20	1.00
8	0.012	0.43	0.20	0.99
6	0.016	0.43	0.20	1.00
4	0.022	0.43	0.19	0.99
2	0.037	N/A	N/A	N/A

elastically-mounted cylinder. They confirmed that the maximum normalized amplitudes of motion collapse very well when plotted against a mass-damping parameter which is defined as:

$$\Lambda \; = \; (m^* + C_A)\, \xi \; , \tag{16}$$

where C_A is the potential added mass coefficient taking a value of 1.0. The authors of this study found that whenever $m^* > 2$ and $\Lambda > 0.006$ simultaneously, the amplitude of motion is fairly constant when Λ remains constant. This offers a great opportunity for the task of validating the robustness and the limitations of the FSI coupling scheme implemented within the FSI solver of the present numerical study. The idea is the following: if Λ remains constant while m^* is reduced, the strength of the fluid-structure interaction increases significantly, but the amplitude of motion is expected to remain constant. As the strength of the FSI increases, the task becomes more and more challenging for the FSI solver, and it can be increased until the coupling scheme becomes numerically unstable. This will allow to investigate the accuracy and the behavior of the solver whenever it is used on the edges of its stability domain.

Using the set of non-dimensional parameters from Table 7, except for U^* which is equal to 5.2, the mass-damping parameter (Λ) is found to be equal to 0.11. Fortuitously, this falls into the aforementioned range of validity of the well-verified approximation where a constant mass-damping (Λ) provides a constant amplitude of motion (A^*_{max}). Using these parameters, a few computations have been achieved with the FSI solver of this study, and Table 10 summarizes the results for the various runs. The results are presented in decreasing order of m^*, which corresponds to an increasing strength of FSI. As observed, the peak amplitude of motion remains constant for all values of m^*, just as much as the values of $C_{y,max}$ and f^*. However, no result is available for the calculation carried out at $m^* = 2$. This is because the simulation becomes unstable due to a too large interaction between the cylinder and the flow for the present explicit solver.

A very interesting observation can be made from these results. Indeed, the values obtained with the FSI solver of this thesis remain accurate even if the strength of the FSI is such that the staggered, explicit coupling scheme is on the edge of its stability domain. Said otherwise, the FSI solver can be considered accurate for whatever strength of the FSI, as long as no instability is encountered.

5. Optimization of the turbine

5.1. Parametric space and initial case

As previously mentioned, a total of seven structural parameters are involved within the equations of motion (Eqs. 1 and 2). Through astute, individual variations of these structural parameters, the dynamics of the airfoil undergoing LCOs can surely be indirectly controlled and tuned in order to impact its efficiency and the amount of power harvested from the flow. Of course, a specific modification may either affect negatively or positively the metrics used to characterize the performances of the device in this study. However, through

an adequate, well-studied choice of each structural parameter, the efficiency of the device, along with the total power harvested, can be increased. An optimization process is required to specifically achieve this.

Two independent performance metrics need to be optimized: one is the previously introduced power coefficient ($\overline{C}_P$), and the other is the harvesting efficiency (η):

$$\eta \;=\; \frac{1}{T}\int_0^T \frac{P}{\frac{1}{2}\,\rho\, U_\infty^3\, bd}\; dt \;, \tag{17}$$

The difference between η and $\overline{C}_P$ is somewhat subtle. In fact, η is the total harvested power normalized by the power available in the flow window harvested by the device, while $\overline{C}_P$ is the total harvested power normalized by a characteristic power based on the chord-length of the foil. *Both* of these metrics need to be optimized in order to obtain an interesting turbine. This is because a very high value of η combined with small amplitudes of motion would result in a low value of $\overline{C}_P$. In this scenario, the device would be very efficient, but very little power would be harvested from the flow.

Having a total of seven adjustable structural parameters implies that the parametric space of the device is huge. Because a FSI simulation requires approximately two to three days of computation, it is impossible to explore the entire parametric space through complete FSI computations. Instead, properly choosing the initial case about which the optimization is to be performed turns out to be much more judicious. Therefore, one needs to determine a set of seven structural parameters representing this well-chosen initial case.

To achieve this, it is wise to use the current knowledge about the kinematically-constrained, flapping-airfoil turbine of the LMFN (see Kinsey & Dumas (2012), Kinsey & Dumas (2008) and Kinsey & Dumas (2006)) . After all, the objective is to optimize the fully-passive turbine in order to achieve the same efficiencies as those of the kinematically-constrained turbine. For this reason, all flow and structural parameters kept constant within this study have been chosen to match the kinematically-constrained device of the LMFN: Re = 500,000, the airfoil is a symmetrical NACA 0015 and $x_{ea} = c/3$.

Nevertheless, the set of seven structural parameters involved within the equations of motion still remains unknown. This is because they have no direct equivalent in the case of the kinematically-constrained turbine. For this reason, an in-house Reverse Passive-Airfoil Solver (RPAS) has been developed in order to approximate the initial value of each structural parameter.

5.2. Reverse Passive-Airfoil Solver (RPAS)

RPAS is an in-house application written in C++ for the specific task of finding a set of structural parameters that is well suited for starting the optimization process. Essentially, RPAS has been designed to solve the reverse mathematical problem of the fully-passive, flapping-airfoil turbine. More details on RPAS are provided in Appendix B.

The objective of RPAS is to find a set of parameters that satisfies as closely as possible the equations of motion over a complete cycle of oscillation. Because the kinematics of the optimal fully-passive airfoil is not known *a priori*, the tabulated kinematics provided as an input to RPAS is that of the kinematically-constrained, flapping-airfoil turbine (see Appendix B for more details). With this, all sets of parameters yielding a relative minimum of the residuals appear suitable at being a proper initial case of the optimization process. It is emphasized that the main idea is to obtain an educated guess of the best initial case minimizing the amount of simulations required to complete the optimization process.

After a thorough analysis of the results obtained from sweeping a realistic parametric space using RPAS, one particular set of parameters has drawn more attention than the others. Its cycle-averaged residuals on both equations of motion were in the range of 8%, and the maximum residuals within a cycle were in the range of 20%. The numerical values of each non-dimensional parameter pertaining to this set are shown in Table 11.

Using this set of parameters, the conventional FSI solver (i.e., the *OpenFOAM* solver) has been used to validate whether or not it constitutes an interesting starting point for the optimization process to follow. To achieve this, a complete FSI simulation has been performed with the parameters of Table 11. The

results are presented in Table 12, together with the values initially used to run RPAS for comparison. The values under the column *RPAS* have been provided as *inputs* to the reverse solver (i.e., they correspond to the targeted motion and performances of the kinematically-constrained turbine), while the values below the column *OpenFOAM* are *outputs* of a complete FSI simulation of the fully-passive airfoil using the case minimizing the residuals.

These results prove that the set of structural parameters described in Table 11 allows the existence of large-amplitude LCOs. Although the performance metrics are not as good as those for the kinematically-constrained device, they are high enough to constitute an interesting starting point for the optimization of the device (see Veilleux (2014) for more details).

6. Optimization methodology and results

A gradient-like optimization has been performed about the initial case previously found using RPAS. This procedure is very systematic and straightforward. Obviously, more refined and elaborate optimization algorithms could have been used for this task, but the simple method presented here proved to be sufficiently efficient. It can be summarized as follows:

1. Individual variations of $\pm$ 10% of each structural parameters are prescribed sequentially about the baseline case, and a complete FSI simulation is performed for each (14 numerical simulations).

2. The values of η and $\overline{C}_P$ are calculated for each of the 14 simulations.

3. The variations are split into two categories: those which affected positively the performances, and those which affected negatively the performances.

4. A simulation combining together all the individual variations which affected positively the performances is carried out. This set of parameters forms the so-called refined case.

5. The values of η and $\overline{C}_P$ are calculated for the refined case.

6. If η and $\overline{C}_P$ of the refined case are greater than the values of η and $\overline{C}_P$ pertaining to the baseline case, the optimization process is performed one more time (proceed to step **1**) with the refined case becoming the new baseline case. If this is not so, proceed to step **7**.

7. The gradient-like optimization is over and a local extrema of η and/or $\overline{C}_P$ has been found.

The results for each solution emerging from the various rounds of optimization are shown in Table 14. As the reader may notice, the results are absolutely great and very promising. Indeed, after performing the optimization process only five times, which implies a total of only 75 calculations, the efficiency and the total power harvested with the fully-passive, flapping-airfoil turbine have been respectively increased by a factor of 2.7 and 3.5. The amplitude of motion and the frequency of oscillation are now much closer to the values of the kinematically-constrained turbine (input values of RPAS shown in Table 12). Further, the values

Table 11: Set of non-dimensional parameters that minimizes the residuals of both equations of motion within the Reverse Passive-Airfoil Solver.

Parameter	Value	Parameter	Value
m_h^*	2.281	S^*	-0.041
k_θ^*	0	k_h^*	1.654
D_θ^*	0.182	D_h^*	1.393
I_θ^*	0.130		

Table 12: Frequency, amplitudes of motion and performances predicted with *OpenFOAM* for the case minimizing the residuals of both equations of motion in the Reverse Passive-Airfoil Solver (RPAS). The values provided as inputs to RPAS (optimal kinematically-constrained turbine) are also indicated for comparison.

Parameter	RPAS (input values)	*OpenFOAM* (output values)
f^*	0.180	0.064
θ_0	80°	62°
y_0^*	1.00	0.94
η	0.430	0.123
$\overline{C}_P$	1.17	0.30

of η and $\overline{C}_P$ drastically increased with each successive optimization, thus leading to performances not so far behind those of the kinematically-constrained, flapping-airfoil turbine. The set of structural parameters corresponding to this last optimized cases, labeled as *Optimization 5*, is described in Table 15. These interesting results tend to prove the feasibility and the great potential of using fully-passive, flapping-airfoil turbines as wind or hydrokinetic turbines, just as the non-passive, kinematically-constrained device. The following subsections examine the physics of the initial and the optimized case in order to explain the better performances of the latter.

Table 13: Set of non-dimensional parameters forming the partially-optimized case resulting from the first round of optimization.

Parameter	Value	Parameter	Value
m_h^*	2.509	S^*	-0.037
k_θ^*	0.026	k_h^*	1.488
D_θ^*	0.164	D_h^*	1.532
I_θ^*	0.117		

6.1. Physics of the initial and the optimized case

The fully-passive, flapping-airfoil turbine making use of the structural parameters forming the initial case oscillates with a reduced frequency (f^*) of 0.064, an amplitude of motion of 62° in pitch (θ_0), and an amplitude of motion of 0.94 chord length in heave (y_0/c). A complementary information to these results and an interesting feature to analyze is the motion history over one complete cycle of oscillation. Note here that the numerical simulations have been computed over enough periods of oscillations so that no distinctive variations are observed from one cycle to the other. For this reason, only the last cycle of oscillation is here considered. This motion history in pitch and in heave is shown in Figure 10, where the effective angle of attack is calculated as:

$$\alpha \;=\; \theta - \arctan\left(\frac{\dot{h}}{U_\infty}\right) \;, \tag{18}$$

A noticeable feature of the motion is perhaps that it is not sinusoidal either for the pitching nor for the heaving motion. Indeed, it has been found through spectral analysis that the second harmonic is very present within both degree-of-freedom signals. A second noticeable feature is the lack of symmetry between

Table 14: Frequency, amplitude of motion and efficiency predicted with *OpenFOAM* for the initial case and for the subsequent optimized cases.

Case	f^*	θ_0	y_0^*	η	$\overline{C}_P$
Initial case	0.064	62°	0.94	0.123	0.300
Optimization 1	0.080	61°	1.02	0.182	0.474
Optimization 2	0.086	68°	1.11	0.242	0.675
Optimization 3	0.090	75°	1.10	0.319	0.896
Optimization 4	0.096	80°	1.27	0.318	0.929
Optimization 5	0.096	83°	1.26	0.336	1.079

Table 15: Set of non-dimensional parameters forming the optimized case resulting from the last round of optimization (optimization 5).

Parameter	Value	Parameter	Value
m_h^*	3.036	S^*	-0.029
k_θ^*	0.031	k_h^*	1.206
D_θ^*	0.119	D_h^*	1.501
I_θ^*	0.095		

the upstroke and the downstroke motion of the airfoil[3]. This will be further analyzed when considering the forces and moments experienced by the airfoil. Concerning α, this quantity will later become useful when analyzing some important features of this case. For the moment, the reader should mostly pay attention to the fact that the peaks of the effective angle of attack and the peaks of the position in heave almost happen at the same moments (i.e., they are in phase or synchronized).

As previously introduced, the energy harvesting efficiency of the initial case (η) is 12.3%, while the coefficient of power ($\overline{C}_P$) is 0.30. Recalling that the effect of a generator connected to the flapping airfoil is modeled here through a linear damping coefficient in heave (D_h), it is also very useful to define another efficiency based on the power dissipated through that linear damper (per unit depth):

$$\eta_{y,damp} = \frac{1}{T} \int_0^T \frac{D_h \dot{h}}{\frac{1}{2}\,\rho\, U_\infty^3\, bd}\, dt\ . \tag{19}$$

The interpretation of this latter parameter is very analog to that of η, except that it provides a performance metric for the *useful* power only. In actual applications, the value of $\eta_{y,damp}$ should remain as close as possible to the value of η.

Using this new definition, a value of $\eta_{y,damp} = 10.3\%$ has been calculated for the current configuration of the turbine. Remembering the value of η to be 12.3%, this indicates that some power is dissipated through the pitch damper, but this represents only a small fraction of the power harvested from the flow: most of the power harvested is provided to the generator. This observation is further confirmed when considering the various coefficients of power previously introduced, the values of which are shown within the schematic

[3]The upstroke is considered to be the part of the cycle where $\dot{h} > 0$, and the downstroke is the portion of the cycle where $\dot{h} < 0$. Also, the beginning of the downstroke formally represents the beginning of a cycle of oscillation ($t/T = 0$).

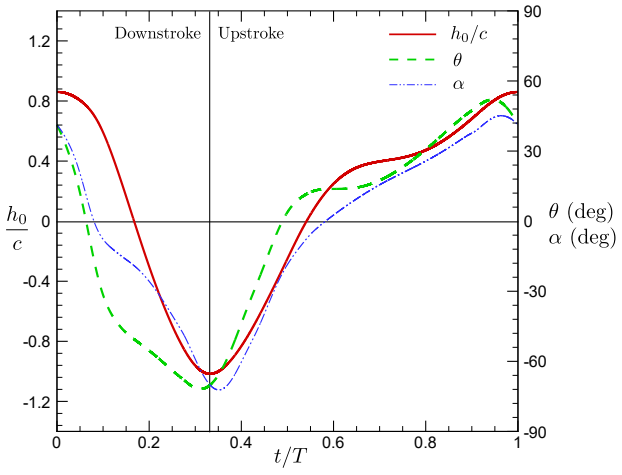

Figure 10: Motions history and effective angle of attack of the fully-passive, flapping-airfoil turbine using the structural parameters of the initial case (see Tables 11 and 12).

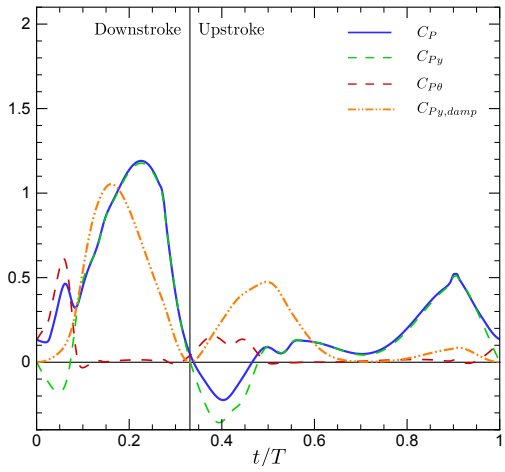

Figure 11: Instantaneous coefficients of power for the fully-passive, flapping-airfoil turbine using the structural parameters of the initial case (Table 11).

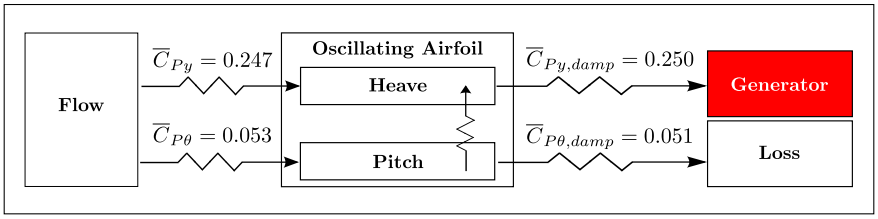

Figure 12: Schematic representation of the flow of power through the fully-passive, flapping-airfoil turbine using the structural parameters of the initial case (Table 11).

representation of Figure 12. As shown, the heaving motion accounts for over 80% of the harvested power. Furthermore, over 80% of the harvested power is provided to the generator. It should also be mentioned that there is a slight internal transfer of energy between both DOFs..

The instantaneous coefficients of power can also be analyzed throughout an entire cycle of oscillation in order to obtain a complete picture of the flow harvesting mechanisms. The instantaneous values of C_P, C_{Py}, $C_{P\theta}$ and $C_{Py,damp}$ are plotted in Figure 11.

A noticeable feature is certainly that the airfoil harvests the flow through the heaving motion for most of the cycle, except for two periods of time: approximately $t/T = 0$ to $t/T = 0.07$ and $t/T = 0.33$ to $t/T = 0.47$. These moments correspond to both transitions between the upstroke and the downstroke. During these, the airfoil is in fact doing some work on the flow through its heaving motion. This, of course, is very costly from a turbine performance point of view. The observed behavior is very different in pitch, where very little power is either harvested from or provided to the flow during most of the cycle. At both transitions between the upstroke and the downstroke, we do observe that some power is harvested from the flow through the pitching motion. In other words, when no power is harvested through the heave, the pitching motion takes over and harvests the flow. As it will soon be highlighted, this is due to the deep dynamic stall of the airfoil. Nonetheless, the contribution of the pitching motion is not always high enough to fully compensate for the work the airfoil is doing on the flow through its heaving motion during these phases, thus leading to negative instantaneous values of C_P. An instantaneous negative value of C_P implies that the turbine, at that specific moment, is doing some work on the fluid. It is thus the inertia of the system that is supplying the power to drive the turbine at that moment. Obviously, this situation is detrimental

from a performance point of view. This is what happens during the transition between the downstroke to the upstroke, between $t/T = 0.33$ and $t/T = 0.47$ in Figure 11

The stalling of the airfoil during its transition from the downstroke to the upstroke ($t/T = 0.33$ to $t/T = 0.47$) can be observed on Figure 13 with the frames corresponding to $t = 4T/12$, $t = 5T/12$ and $t = 6T/12$. This figures shows the normalized z-vorticity fields in the vicinity of the airfoil at various equally-spaced moments of the cycle. A large eddy shed from the leading edge of the airfoil is clearly present. However, the motion of the airfoil during the transition between the downstroke to the upstroke is such that the airfoil's surface does not remain close to the vortex as it is convected downstream: once the eddy is shed, the airfoil starts moving very quickly in the opposite direction due to the effect of the spring in heave, thus taking the airfoil away from the vortex. This certainly restrains the level of interaction between the vortex and the airfoil, thus reducing the work achieved by the flow on the airfoil. Despite this observation, the vortex does play an important role in the cycle: since no spring is present in pitch (see Table 11), the pitching of the airfoil during the transition from the downstroke to the upstroke mostly depends on this airfoil-vortex interaction.

The reader should now return briefly to Figure 10 and consider the curve for the effective angle of attack and the curve for the heave position around $t/T = 0.33$ to $t/T = 0.47$. Because the large vortex is approximately shed when the maximum effective angle of attack is reached, it clearly appears that the airfoil is already moving upward when the shedding happens. This confirms the inadequate synchronization between the heaving motion and the pitching motion.

Conversely, during the transition of the airfoil from the upstroke to the downstroke ($t/T = 0$ to $t/T = 0.07$), the large vortex shed at the leading edge remains closer to the airfoil's surface as it is convected downstream. This is observed with the frames corresponding to $t = 11T/12$, $t = 0$ and $t = T/12$ in Figure 13. This can also be noted by considering the effective angle of attack and the heave position shown in Figure 10. Again, the shedding of the vortex approximately occurs at the extremum value of the effective angle of attack. As this happens, the airfoil continues to move towards the vortex for some time, before to start moving in the opposite direction, away from the vortex. The airfoil-vortex interaction is therefore greater than what has been observed during the transition from the downstroke to the upstroke, and this has positive effects overall. Indeed, as the vortex remains closer to the leading edge and moves downstream, the low pressure it causes on the airfoil's surface beyond the elastic axis leads to a fairly large pitching moment. This, combined with a fairly large pitching rate at the same moment, results in a relatively large power harvested from the flow through the pitching motion. In fact, the harvesting of the flow through the pitching motion is large enough to fully compensate for the work done on the flow through the heaving motion of the airfoil at the same moment, thus leading to an overall positive instantaneous value of C_P.

The fact that the airfoil is doing some work on the flow through its heaving motion at both the upstroke and the downstroke extrema is also associated to an inadequate synchronization between the heaving and the pitching motions: as the airfoil reverts direction in heave, the lift is such that it is opposed to the airfoil's motion. To summarize, in the present case the airfoil changes direction in heave mainly as a result of the structural stiffness in heave. In the best scenario, the sign of the lift and the sign of the heaving velocity should change at the same moment.

The budget of all terms involved within the equations of motion is shown in Figure 14. The value of each term is computed according to the following equations:

$$C_{\mathcal{L}} \; - \; 2m_h^* \, \ddot{h}^* \; - \; 2S^* \left(\dot{\theta}^{*2} \sin\theta - \ddot{\theta}^* \cos\theta \right) \; - \; 2D_h^* \, \dot{h}^* \; - \; 2k_h^* \, h^* \; = \; 0 \; , \tag{20}$$

$$C_M \; - \; 2I_\theta^* \, \ddot{\theta}^* \; + \; 2S^* \ddot{h}^* \cos\theta \; - \; 2D_\theta^* \, \dot{\theta}^* \; - \; 2k_\theta^* \, \theta \; = \; 0 \; . \tag{21}$$

These are simply the equations of motion where all terms have been switched to the left-hand side. As a result, the summation of all contributions, at any moment in the cycle, is equal to zero.

The effect of deep dynamic stall is visible on both $C_{\mathcal{L}}$ and C_M. As previously mentioned, the effect of the shed vortex is mitigated for $t/T = 0.33$ to $t/T = 0.47$. However, the vortex has a relatively large impact on the aerodynamics in the vicinity of $t/T = 0$ to $t/T = 0.07$, and this is especially clear when considering the aerodynamic moment where a sharp peak is observed. However, it is worth repeating that the pitching

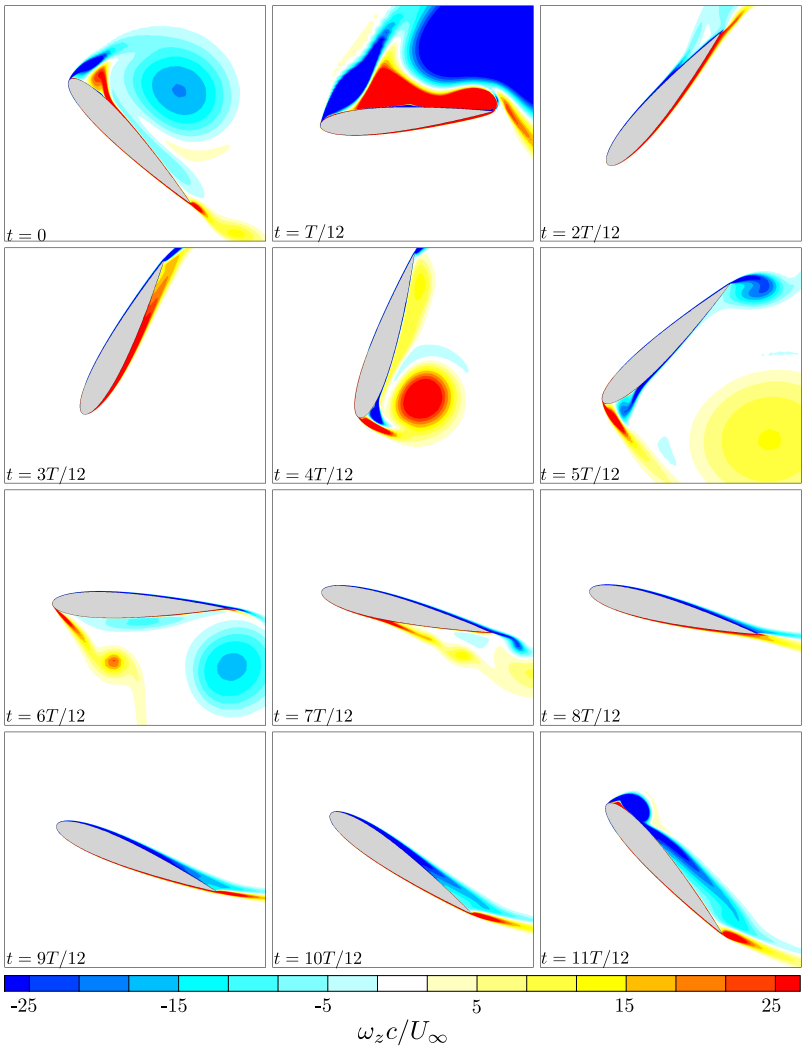

Figure 13: Fields of normalized z-vorticity ($\omega_z c/U_\infty$) in the vicinity of the flapping airfoil at various instants throughout one complete period of oscillation (T) for a fully-passive, flapping-airfoil turbine using the structural parameters of the initial case (Table 11).

of the airfoil at the end of both the upstroke and the downstroke is attributed to the interaction between the vortex and the airfoil, which means that although the interaction is weaker for $t/T = 0.33$ to $t/T = 0.47$, there is obviously one, and it is not negligible. Indeed, it is precisely when the vortex generates a fairly low pressure on the airfoil, close to the trailing edge, thus giving rise to a moderate/strong aerodynamic moment, that the airfoil starts pitching in the opposite direction. This synchronization can be observed if the reader compares the motion history of Figure 10 with the history of C_M from Figure 14b. This highlights the large impact of the vortex shed during the deep dynamic stall event. The fact that the airfoil-vortex interaction is so important indicates that the airfoil is undergoing LCO as a result of stall flutter: it is the periodic stalling of the airfoil that prevents the motion from simply diverging from the equilibrium position, thus leading to the cyclic motion.

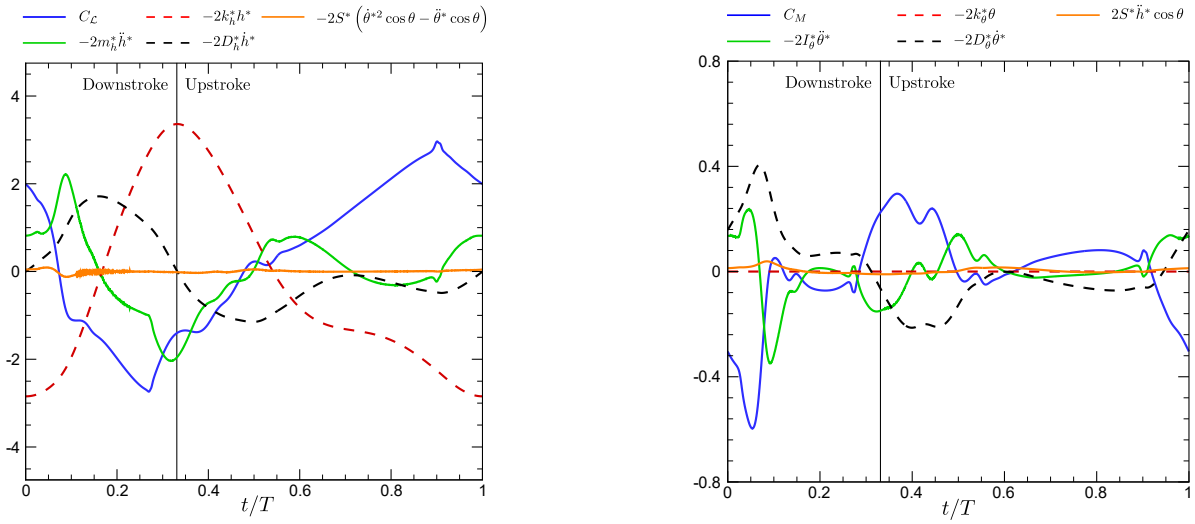

(a) Heave motion

(b) Pitch motion

Figure 14: Budget of the terms involved within the equation of motion in heave of the fully-passive, flapping-airfoil turbine using the structural parameters of the initial case (Table 11).

6.2. Optimized case

Moving on to the optimized case (see Table 15), a reduced frequency (f^*) of 0.096 has been obtained, combined with amplitudes of motions in pitch (θ_0) and in heave (h_0/c) of respectively 83° and 1.26 chord length. It is noticeable that the motion in heave is very close to being sinusoidal. Nevertheless, this is not the case for the pitching motion. Indeed, the pitching motion happens in three distinct phases during the cycle. First, there is a phase where the pitching rate is relatively constant and takes a fairly high value (the "fast pitching regime"). There is another phase where the pitching rate is again relatively constant, but takes a much lower value than previously (the "slow pitching regime"). Lastly, there is another phase where the pitching rate is not constant (the "transitional pitching regime"). This happens during both transitions between the upstroke and the downstroke. Another feature that can be observed on Figure 15 is the great symmetry between the downstroke and the upstroke. This is obviously in contrast with the results of the previously analyzed initial case.

For this optimized configuration of the fully-passive, flapping-airfoil turbine, a very interesting value of 33.6% has been computed for η, and a value of 1.079 has been obtained for $\overline{C}_P$. The same metrics as those used within the previous subsection can also be used in order to better understand how the turbine is harvesting the flow. It is found that $\eta_{y,damp}$ takes a value of 29.1%, which means that most of the harvested power is again provided to the generator and very little is lost in the pitch damper. Again, this is the desired behavior since only the power available to the generator is considered as being useful. The fact that most of the harvested power is indeed useful is further highlighted with a schematic of the coefficients of power characterizing the turbine. This is shown in Figure 17. It can be observed that over 85% of the power is harvested through the heaving motion of the turbine. Furthermore, over 85% of the total harvested power is useful and available to the generator. A very small value of $\overline{C}_{P,tr} = 0.009$ has been calculated. Again, this corresponds to what is transferred from the pitch degree-of-freedom to the heave degree-of-freedom. This is the same situation as the one observed for the initial case: the pitch degree-of-freedom feeds very little power to the heave degree-of-freedom, thus providing only slightly more power to the generator than what is harvested through the heave motion. Furthermore, these results demonstrate that the pitching motion can be fully autonomous from an energetic point of view. Indeed, the power dissipated within the pitch damper is fully compensated by the power harvested through the pitch motion.

The instantaneous values of the most important coefficients of power, namely C_P, C_{Py}, $C_{P\theta}$ and

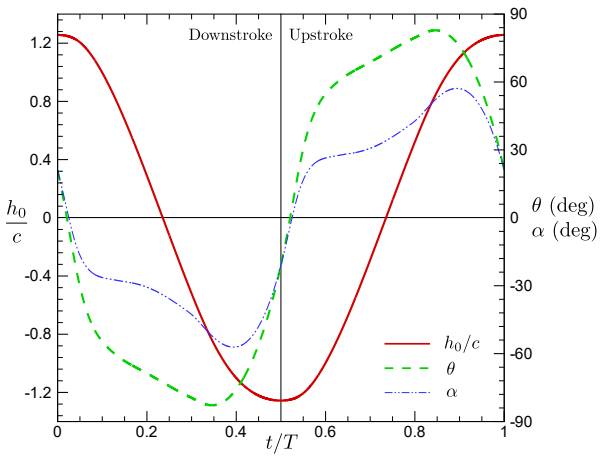

Figure 15: Motion history and effective angle of attack of the fully-passive, flapping-airfoil turbine using the structural parameters of the optimized case (see Tables 14 and 15).

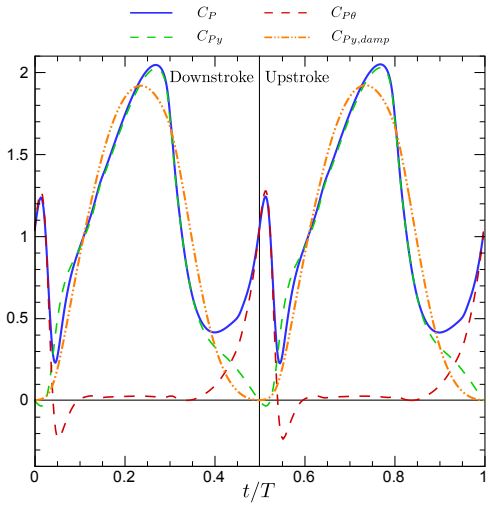

Figure 16: Instantaneous coefficients of power for the fully-passive, flapping-airfoil turbine using the structural parameters of the optimized case (Table 15).

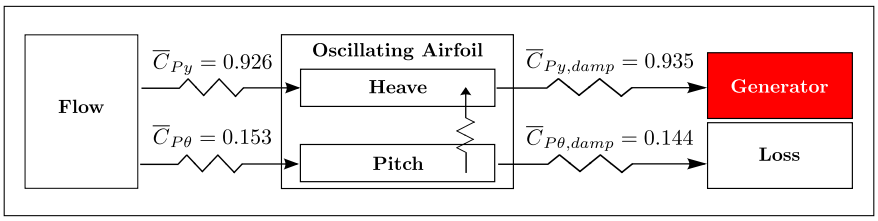

Figure 17: Schematic representation of the flow of power through the fully-passive, flapping-airfoil turbine using the structural parameters of the optimized case (Table 15).

$C_{Py,damp}$, have also been computed and plotted throughout a complete cycle of oscillation. This is shown in Figure 16. The first noticeable difference with respect to the initial case certainly resides in the far larger values of the power coefficients that are reached with the optimized turbine. This, of course, is in agreement with the fact that more power is harvested with the optimized turbine.

Furthermore, the curve of C_P indicates that the device harvests the flow at *all* moments throughout its cycle: there is no portion of the cycle where the flapping airfoil is doing some work on the flow (negative C_P). This is in contrast with the initial case, where the airfoil did provide some work on the flow at some moments of the cycle. In addition, the curve of C_P exhibits four distinctive peaks. Two of them are identical and of lower amplitude (peak value of 1.3), and two of them are identical and of larger value (peak value of 2.05). The two peaks with a larger amplitude correspond to the portion of the cycle where the airfoil is approximately in the middle of its downstroke or of its upstroke and has a large heaving velocity. The curves of C_P and C_{Py} are very close to each other near these two peaks. During these moments where the airfoil's heaving velocity is great, the pitching motion, in counterpart, does not contribute at harvesting the flow significantly, nor does it do some work on the flow. It is therefore the heaving motion that accounts for these peaks of large amplitude.

In contrast, the peaks of lower amplitude happen when the airfoil is transitioning from the downstroke to the upstroke, and vice versa. The peaks are associated to the deep dynamic stall events happening at both extrema of the heaving motion. It can be observed that in the vicinity of $t/T = 0.45$ to $t/T = 0.55$ and

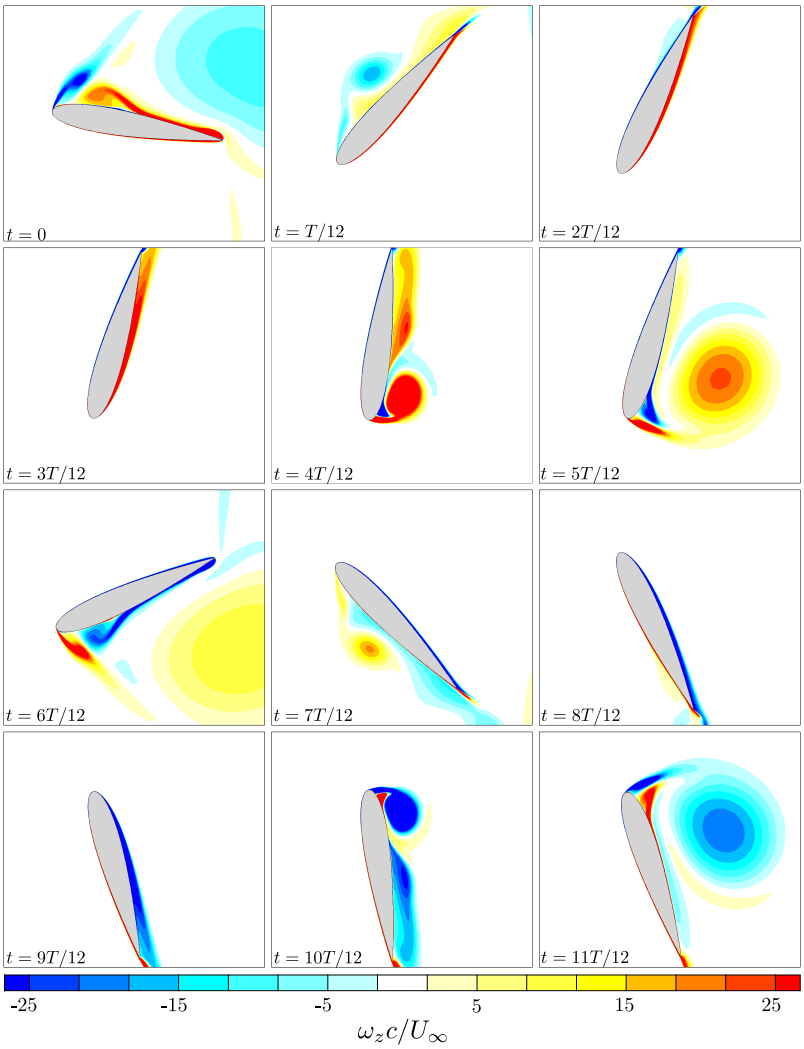

Figure 18: Fields of normalized z-vorticity ($\omega_z c/U_\infty$) in the vicinity of the flapping airfoil at various instants throughout one complete period of oscillation (T) for the fully-passive, flapping-airfoil turbine using the structural parameters of the optimized case (Table 15).

$t/T = 0.95$ to $t/T = 0.05$ the curves of C_P and $C_{P\theta}$ are very close to each other, thus indicating that very little or no harvesting of the flow is achieved through the heaving motion. This makes physical sense as the heaving velocity is relatively small during these transitions between the downstroke and the upstroke. It is indeed the pitching motion alone that accounts for these two smaller peaks on the curve of C_P . The effect of the dynamic stall happening at these moments can also be seen in Figure 18 where the z-vorticity fields are shown in the vicinity of the airfoil at various moments within a complete cycle of oscillation. The first stalling event, corresponding to the transition between the downstroke to the upstroke, can be visualized with the frames for $4T/12$, $5T/12$ and $6T/12$. The second stalling event, corresponding to the transition between the upstroke to the downstroke, can be observed on the frames at $10T/12$, $11T/12$ and 0.

It should be observed that the interaction of the shed vortex with the airfoil is very important during the deep dynamic stall events. As the eddy travels downstream, it remains very close to the airfoil's surface, thus generating a relatively intense low pressure on one side of the airfoil. This is also visible when considering the aerodynamic forces and moments on the airfoil, which are shown in Figure 19. This figure shows the budget

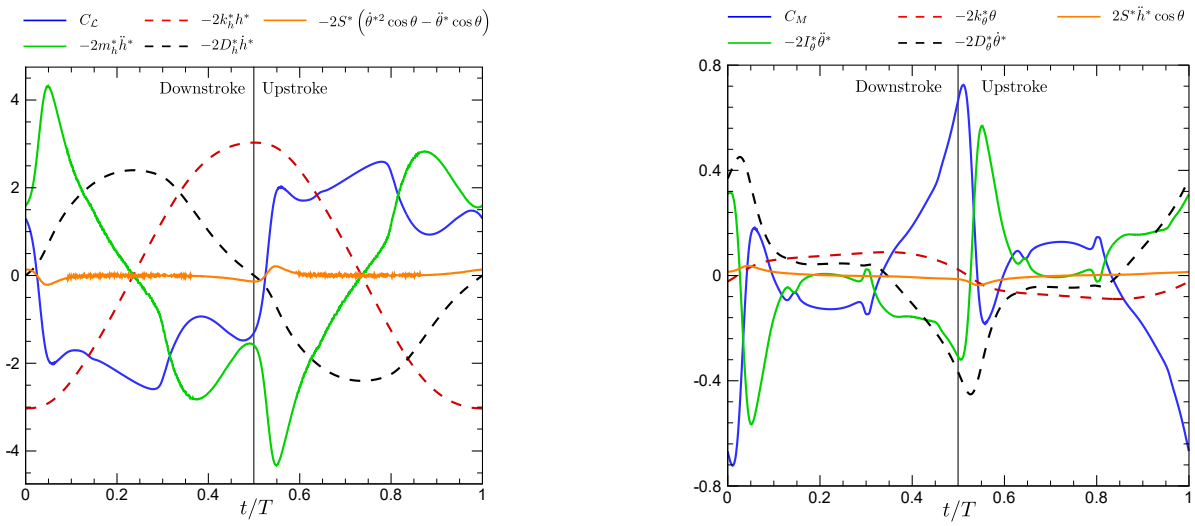

(a) Heave motion

(b) Pitch motion

Figure 19: Budget of the terms involved within the equation of motion in heave of the fully-passive, flapping-airfoil turbine using the structural parameters of the optimized case (Table 11).

of all terms involved within both equations of motion, just as for Figure 14. Following the deep dynamic stall event, the value of $C_{\mathcal{L}}$ drops significantly, followed by a partial and momentarily re-augmentation. This re-augmentation of the lift force is due to the low pressure that exists within the core of the vortex. The interaction between the eddy and the airfoil is also very clear from the curve of C_M. The large peaks are again due to the airfoil-vortex interaction. As the eddy travels downstream, the arm of the forces generated by the eddy on the airfoil increases, and it generates a fairly large aerodynamic moment on the airfoil.

This strong interaction between the airfoil and the vortex is the result of an adequate synchronization between the pitching and the heaving motions, which is very different from what has been observed for the initial case. Indeed, the current motion is such that the vortex remains close the the airfoil's surface for both the upstroke and the downstroke. When the vortex is shed, the airfoil continues to travel towards the vortex, thus keeping it close enough to interact greatly with it. By considering the heave position in time and the effective angle of attack in time, which are shown in Figure 15, this becomes obvious. Because the vortex is approximately shed when the airfoil reaches its peak value of the effective angle of attack, it is clear that the airfoil travels for some time towards the vortex after it is shed. This is because the peak values of the effective angle of attack happen significantly before the peak values of the heave position.

This strong interaction with the vortex allows the airfoil to use the low pressure at the core of the eddy to passively pitch the airfoil and to extract more power from the flow. One could have believed that the presence of a spring in pitch is the governing agent of the airfoil's pitching motion, but it turns out that this is clearly not the case. It is obvious from Figure 19b that it is the interaction with the vortex that is mainly responsible for the pitching of the airfoil at the extrema of the upstroke and the downstroke. Indeed, the moments generated by the spring are approximately one order of magnitude smaller than the moments associated to the airfoil-vortex interaction. Furthermore, the reader can verify that the large aerodynamic moment corresponds precisely to the moment where the airfoil is in the fast pitching regime. Again, this confirms that stall flutter is definitely the physical mechanism through which the amplitude of motion of the airfoil is limited, thus leading to a periodic motion.

The adequate synchronization between both motions also has another positive effect on the efficiency of the device. Returning to Figure 16, it is observed that the heaving motion of the airfoil never actually does work on the flow. This is because the lift coefficient and the heaving velocity change sign at the same moment, and this does not lead to the detrimental situation where the lift and the heaving velocity are in

opposite directions. This adequate synchronization can be appreciated from Figure 15.

Returning to the fast and the slow pitching regimes of the airfoil, these turn out to have another very significant and positive impact on the performances of the turbine. Indeed, the curve of $C_{\mathcal{L}}$, which is shown in Figure 19a, is very different from that of the initial case shown in Figure 14a. Because the airfoil exhibits a fast pitching regime right after it has transitioned from the upstroke to the downstroke, or vice versa, the lift coefficient quickly reaches fairly high values, thus maximizing the power harvested through heaving. If the pitching of the airfoil were to happen slowly at the beginning of the upstroke or the downstroke, such as if the pitching was sinusoidal in time, the value of the lift coefficient would remain much lower for a significant portion of the cycle, which would necessarily imply a lower value of the power extracted from the flow. To make this point clear, the idea here is that the fast pitching regime minimizes the impact of the transition from the upstroke to the downstroke, and vice versa. Obviously, the lift force has to take a null value at some point during this transition, but the lift should not remain close to this value for long. The fast pitching regime achieves exactly this task by increasing the lift very quickly.

As a last comment, it is interesting to note that the inertial coupling term shown in Figure 19 is again of mitigated importance when compared to all other terms involved within both equations of motion of the fully-passive, flapping-airfoil turbine. This suggests that this coupling term did not play a significant role in the optimization process.

6.3. Theoretical analysis of the airfoil's loss of stability

Divergence is a static instability which happens whenever the torsional restoring moment is not large enough to counteract the aerodynamic moment. Said otherwise, the aerodynamic moment grows faster than the restoring moment from the spring. The ratio of the dynamic pressure at divergence over the dynamic pressure is:

$$\frac{q_{div}}{q} = \frac{2\,c\,k_{\theta}^{*}}{e\left(\dfrac{\partial C_{\mathcal{L}}}{\partial \theta}\right)}\,, \tag{22}$$

where e is the distance between the aerodynamic center and the elastic axis (see Dowell et al. (2005)). This ratio is formally equal to 0 for the initial case, and approximately equal to 0.12 for the optimized case. This means that the optimized airfoil is statically unstable due to the divergence phenomenon.

This last result suggests that the LCO of the airfoil are not only self-sustained, but they are also self-induced. Indeed, following any perturbation, as small as it can be, the airfoil starts diverging from its equilibrium position. Once it reaches a large amplitude in both pitch and heave, a deep dynamic stall event occurs, thus limiting the divergence of the airfoil by forcing it to start moving in the opposite direction. This is the process through which the cyclic motion is initiated, and preliminary experimental testing currently under way has confirmed this theoretical observation (Boudreau et al. (2016)). It has been verified that the airfoil does enter the LCO regime when no external perturbation is provided.

7. Conclusion

This paper is a fairly extensive initial investigation of a hydrokinetic turbine making use of the self-sustained, pitch-heave oscillations of an elastically-mounted, symmetrical and rigid airfoil. Such a novel type of flow harvester could prove to be very useful as a result of its relatively simple mechanics when compared to other sorts of hydrokinetic turbines, and it appears to be well adapted for harvesting a water flow of limited depth. The present numerical work is among the first few studies to extensively consider a fully-passive, flapping-airfoil turbine, especially for high Reynolds numbers that are representative of a realistic turbine application.

It has been shown that the strongly coupled equations of motion involve a total of seven structural parameters. All of these parameters can be individually varied as a way to indirectly control the motion of the flapping-airfoil. Through modifications of the airfoil's dynamics, its performances at harvesting a

freestream flow can also be modified. Therefore, it is possible to optimize the turbine through an astute choice of each individual parameter.

In order to initiate this optimization process of the turbine with a well-chosen initial case, a clever methodology has been implemented with an in-house application. The objective of the Reverse Passive-Airfoil Solver is to solve the inverse mathematical problem where the kinematics and the aerodynamics are prescribed. With such a methodology, an initial case having an efficiency in the range of 12% has been obtained. Following this, a gradient-like optimization has been carried out about this initial case, thus increasing the efficiency to 34%. Such an efficiency demonstrates that there is obviously good potential at using fully-passive, flapping-airfoils for the purpose of harvesting a flow.

Two mechanisms have been identified as being responsible for the great performances of the optimized case at harvesting a flow. First, the adequate synchronization between the pitching and the heaving motion is a crucial element. This is because an adequate synchronization does prevent the airfoil from doing work on the flow at some moments of its cycle, thus loosing energy rather than harvesting it, and it allows the airfoil to remain closer to the vortex shed during the deep dynamic stall, thus enhancing the beneficial airfoil-vortex interaction. The second mechanism is the presence of a fast pitching regime. Because the airfoil must necessarily experience a null effective angle of attack when it reaches an extrema in heave, the lift coefficient must also be momentarily null. Because of the fast pitching regime, the effective angle of attack does not remain close to zero for too long, and the lift coefficient quickly becomes large again. This minimizes the effect of changing the heaving direction, and the larger lift coefficients resulting from such a motion enhance the harvested power from the flow.

Following the present numerical study, it will be important to consider three-dimensional numerical simulations in order to refine the numerical predictions. Future studies should also deal with the effect of the location of the elastic axis. Xiao & Zhu (2014) showed that moving the elastic axis can have a significant impact on a passive airfoil. In fact, they suggest that moving the location of the elastic axis is equivalent to changing the phase lag between the heaving and the pitching motions, and the current study shows that this synchronization is a critical parameter. Another structural parameter that should be investigated is the airfoil's profile.

Last but not least, a *semi-passive*, flapping-airfoil turbine could be investigated. Studying the fully-passive turbine surely provided a very good understanding of the physics involved, but a semi-passive turbine where only one degree-of-freedom is prescribed could be studied. In fact, the semi-passive devices that have been studied so far in the literature are aeroelastic apparatus where the pitch is prescribed and the heave results from the fluid-structure interaction. However, a novel system where the heave is prescribed and the pitch results from the fluid-structure interaction could be studied more deeply. Indeed, if a linear motor/generator was connected to the airfoil, it could be used to constrain the heaving motion. Then, the structural parameters of the device could be adjusted in order to obtain an efficient pitching motion. Such a semi-passive turbine where the linear motor/generator is used to control the motion could most probably be more easily optimized than its fully-passive counterpart. This is because a linear motor/generator could provide a damping force that is variable throughout the cycle, thus providing much control over the airfoil's motion. Last, the semi-passive device where the heaving motion is constrained has a clear advantage over the semi-passive device where the pitch is constrained. Because the generator must be connected to the heaving motion, constraining the heaving motion means that only one motor/generator is needed. On the contrary, constraining the pitching motion requires a motor for the pitching motion, as well as a generator for the heaving motion.

Acknowledgements

Financial support from NSERC Canada (RGPIN grant and CGS-D scholarship) is gratefully acknowledged by the authors. Expert revision of the manuscript by Matthieu Boudreau of the LMFN is also gratefully acknowledged. Computations in this study were performed on the Colosse supercomputer in the HPC network of Calcul Québec under the auspices of Compute Canada.

Appendix A Modeling of the generator

The modeling of the energy sink mimiking the presence of an electric generator connected to the oscillating foil has been addressed here by considering a viscous type of damping. This subsection does not aim at being an exhaustive review of the theory concerning electrical generators. The interested readers may find more details within references dedicated to this matter, such as Abad et al. (2011); Tan (2011); Wildi & Sybille (2000) and Wu et al. (2011). Nevertheless, a simple analysis can be done in order to justify and bring some support to the generator's model used in this study. To begin with, the voltage (E_0) induced by a generator through Faraday's induction, according to Wildi & Sybille (2000), is given by:

$$E_0 \;=\; \frac{Zn\phi_p}{60} \;, \tag{23}$$

where Z is the number of conductors in the armature, n is the armature revolution in RPM (rotations per minute) and ϕ_p is the flux per pole of the generator. Furthermore, the required torque to activate the generator (T_g) is given by:

$$T_g \;=\; \frac{Z\phi_p I}{2\pi} \;, \tag{24}$$

where I is the current produced by the generator. A generator under an electrical load can be represented with the simple equivalent circuit shown in Figure 20, where R_0 is the internal resistance of the generator, and R_L is the resistance of the load. With this circuit, the value of the current can easily be found:

$$I \;=\; \frac{E_0}{R_0 + R_L} \;. \tag{25}$$

Combining Eqs. 23 to 25, an expression for the torque is then obtained:

$$T_g \;=\; \frac{Z^2\phi_p^2\, n}{120\pi\,(R_0 + R_L)} \;. \tag{26}$$

Returning to the aeroelastic model of this study, the generator's damping force on the heave motion simply corresponds to the torque required to drive the generator divided by some arm length, the value of which depends upon the specific configuration of the apparatus. In addition, one can reasonably assume that, the angular velocity of the generator's armature (n) is proportional to the heaving velocity ($\dot{y}$). With this, the following can be written:

$$F_{damp} \;=\; \left[\frac{KZ^2\phi_p^2}{120\pi\,(R_0 + R_L)}\right]\dot{y} \;, \tag{27}$$

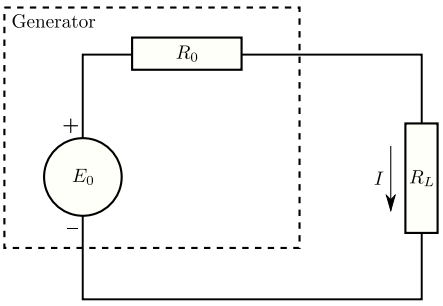

Figure 20: Equivalent circuit for an electrical generator under an electrical load.

where F_{damp} is the damping force and K is a proportionality constant. The interesting point here is to realize that the previous equation can be written in the following form:

$$F_{damp} \;=\; D_h \dot{y} \;, \tag{28}$$

This shows that for a constant electrical load and a constant flux within the generator, a viscous type of damping indeed models adequately the effect of a generator connected to the fully-passive, flapping-airfoil turbine. This confirms that the simple model used in this research is realistic and certainly not far fetched. It also demonstrates that the specific value of the damping coefficient can be changed by varying the electrical load, as much as through modulations of the flux ϕ_p.

Appendix B Reverse Passive-Airfoil Solver (RPAS) – More Details

RPAS is an in-house application written in C++ for the specific task of finding a set of structural parameters that is well suited for starting the optimization process. Essentially, RPAS has been designed to solve the reverse mathematical problem of the fully-passive, flapping-airfoil turbine. To highlight what this means, we first recall that for the *conventional* FSI solver (i.e., the *OpenFOAM-2.1.x* solver), the following is achieved for each run:

- A total of seven structural parameters are chosen (input);
- The flow parameters are chosen (input);
- The equations of the flow and the dynamics equations for the foil are solved using *OpenFOAM*;
- The results are the foil's kinematics and the aerodynamic coefficients (output), thus allowing to calculate the performances of the turbine.

Therefore, the aerodynamics and the kinematics of the LCOs are an *output* of the conventional solver. This is the opposite of what happens while solving the reverse mathematical problem, which can be summarized in the following way:

- The airfoil's kinematics and aerodynamics are chosen, tabulated and provided to RPAS (input);
- The possible ranges of values of the structural parameters are chosen (input);
- The solver computes the residuals of the equations of motion over all the possible sets of structural parameters among the allowed ranges of values, and it records the residuals pertaining to each equation of motion;
- The set(s) of structural parameters that minimizes the residuals of both equations (relative minimum) is obtained (output).

To explain in more details, the RPAS software enables the user to specify a range and an increment for each structural parameter. Through this, the user specifies which portion of the parametric space is investigated, as much as the resolution used to perform the numerical investigation. The user also provides RPAS with the airfoil's tabulated kinematics ($h^*(t^*)$, $\dot{h}^*(t^*)$, $\ddot{h}^*(t^*)$, $\theta(t^*)$, $\dot{\theta}(t^*)$ and $\ddot{\theta}(t^*)$) along with the corresponding tabulated aerodynamics ($C_{\mathcal{L}}(t^*)$ and $C_M(t^*)$) over one complete cycle of oscillation (obtained through experimental data or CFD as in this case). With this in hand, the solver iterates over each possible combination of seven structural parameters within the specified parametric space. For each set of parameters, all the variables of the equations of motion (Eqs. 1 and 2) are known. However, there is a residual to these equations. In other words, the aerodynamics, the kinematics and the structural parameters do not fully and exactly satisfy the equations of motion. The residuals are computed in the following way:

$$R_{\mathcal{L}} \;=\; \frac{m_h\,\ddot{y} \;+\; S\left(\dot{\theta}^2\,\sin\theta - \ddot{\theta}\cos\theta\right) \;+\; D_h\,\dot{y} \;+\; k_h\,y \;-\; C_{\mathcal{L}}}{(C_{\mathcal{L}})_{max}}\;, \tag{29}$$

$$R_M \;=\; \frac{I_\theta\,\ddot{\theta} \;-\; S\,\ddot{y}\,\cos\theta \;+\; D_\theta\,\dot{\theta} \;+\; k_\theta\,\theta \;-\; C_M}{(C_M)_{max}}\;, \tag{30}$$

and they are computed at various instants throughout the cycle of oscillation for each set of structural parameters.

Because the kinematics of the optimal fully-passive airfoil is not known *a priori*, the tabulated kinematics provided as an input to RPAS is that of the kinematically-constrained, flapping-airfoil turbine with an amplitude of motion in pitch (θ_0) of 80°, with an amplitude of motion in heave (h_0^*) of 1 chord length, and with a reduced frequency (f^*) of 0.18 and a phase of 90° between both motions. These metrics correspond to an optimal case of the kinematically-constrained turbine (η of 43%). The tabulated kinematics can be summarized with the following equations:

$$\theta(t^*) \;=\; \theta_0 \sin\left(2\pi f^*\,t^*\right)\;, \tag{31}$$

$$y^*(t^*) \;=\; y_0^* \sin\left(2\pi f^*\,t^* + \frac{\pi}{2}\right)\;. \tag{32}$$

OpenFOAM-2.1.x has been used for the task of predicting the forces and moments on the NACA 0015 airfoil undergoing the motion described with Eqs. 31 and 32. The forces and moments obtained have also been compared with those of Kinsey from the authors' group LMFN (private communication and Kinsey & Dumas (2014)).

The last inputs needed by RPAS to perform the residuals scan are the range and increment for each structural parameter. A first raw and fairly permissive estimation of some realistic and practical range of values has been proposed through dimensional considerations of a real turbine. This parametric space has been investigated with RPAS using a coarse increment between each successive value taken by a given parameter. Following this first sweep, some regions of the parametric space where the residuals of both equations were lower have been identified. Within these regions, a second sweep making use of a refined increment between successive values has been carried out.

References

Abad, G., Lpez, J., Rodrguez, M., Marroyo, L., & Iwanski, G. (2011). *Doubly Fed Induction Machine: Modeling and Control for Wind Energy Generation*. Hoboken, New Jersey: Wiley.

Anagnostopoulos, P., & Bearman, P. W. (1992). Response characteristics of a vortex-excited cylinder at low reynolds numbers. *Journal of Fluids and Structures*, *6*, 39–50.

Bhardwaj, R., & Mittal, R. (2012). Benchmarking a coupled immersed-boundary-finite-element solver for large-scale flow induced deformations. *AIAA Journal*, *50*, 1638–1642.

Boudreau, M., Dumas, G., & Oshkai, P. (2016). private communication.

Causin, P., Gerbeau, J., & Nobile, F. (2005). Added-mass effect in the design of partitioned algorithms for fluid-structure problems. *Computer Methods in Applied Mechanics and Engineering*, *194*, 4506–4527.

Degroote, J., Bruggeman, P., Haelterman, R., & Vierendeels, J. (2008). Stability of a coupling technique for partitioned solvers in FSI applications. *Computers and Structures*, *86*, 2224 – 2234.

Dimitriadis, G., & Li, J. (2009). Bifurcation behavior of airfoil undergoing stall flutter oscillations in low-speed wind tunnel. *AIAA Journal*, *47*, 2577–2596.

Dowell, E. H., Clark, R., Cox, D., Curtiss, H. C., Edwards, J. W., Hall, K. C., Peters, D. A., Scanlan, R., Simiu, E., Sisto, F., & Strganac, T. W. (2005). *A Modern Course in Aeroelasticity* volume 116 of *Solid Mechanics and Its Applications*. (4th ed.). Dordrecht, The Netherlands: Springer Netherlands.

Farrell, P. E., & Maddison, J. R. (2011). Conservative interpolation between volume meshes by local Galerkin projection. *Computer Methods in Applied Mechanics and Engineering*, *200*, 89–100.

Ferziger, J., & Perić, M. (2002). *Computational Methods for Fluid Dynamics*. (3rd ed.). Springer.

Förster, C., Wall, W., & Ramm, E. (2007). Artificial added mass instabilities in sequential staggered coupling of nonlinear structures and incompressible viscous flows. *Computer Methods in Applied Mechanics and Engineering*, *196*, 1278 – 1293.

Fortin, A. (2001). *Analyse numrique pour ingnieurs*. (2nd ed.). Presses internationales Polytechnique.

Guney, M., & Kaygusuz, K. (2010). Hydrokinetic energy conversion systems: A technology status review. *Renewable and Sustainable Energy Reviews*, *14*, 2996–3004.

He, T., Zhou, D., & Bao, Y. (2012). Combined interface boundary condition method for fluid-rigid body interaction. *Computer Methods in Applied Mechanics and Engineering*, *223-224*, 81–102.

Huxham, G. H., Cochard, S., & Patterson, J. (2012). Experimental Parametric Investigation of an Oscillating Hydrofoil Tidal Stream Energy Converter. In *18th Australasian Fluid Mechanics Conference*. Launceston, Australia.

Julien, S., Dumas, G., & Mtivier, V. (2007). URANS Simulations of High Amplitude Flapping Airfoils. In *15th Annual Conference of the CFD Society of Canada*. Toronto, Canada. Paper CFD-2007-1117.

Kinsey, T., & Dumas, G. (2006). Parametric study of an oscillating airfoil in power extraction regime. In *24th AIAA Applied Aerodynamic Conference*. San-Francisco, California.

Kinsey, T., & Dumas, G. (2008). Parametric Study of an Oscillating Airfoil in a Power-Extraction Regime. *AIAA Journal*, *46*, 1318–1330.

Kinsey, T., & Dumas, G. (2012). Computational fluid dynamics analysis of a hydrokinetic turbine based on oscillating hydrofoils. *Journal of Fluids Engineering*, *134*.

Kinsey, T., & Dumas, G. (2014). Optimal Operating Parameters for an Oscillating Foil in Power-Extraction Regime at Reynolds Number 500,000. *AIAA Journal*, *52*, 1885–1895. doi:10.2514/1.J052700.

Kinsey, T., Dumas, G., Lalande, G., Ruel, J., Mehut, A., Viarouge, P., Lemay, J., & Jean, Y. (2011). Prototype testing of a hydrokinetic turbine based on oscillating hydrofoils. *Renewable Energy*, *36*, 1710–1718.

Lapointe, S. (2012). *Numerical study of self-sustained oscillations in transitional flows*. Master's thesis Université Laval.

Lapointe, S., & Dumas, G. (2011). Improved Numerical Simulations of Self-Sustained Oscillations of a NACA0012 with Transition Modeling. In *41st AIAA Fluid Dynamics Conference*. Honolulu, Hawai. Paper AIAA-2011-3528.

Lapointe, S., & Dumas, G. (2012). Numerical Simulations of Self-Sustained Pitch-Heave Oscillations of a NACA0012 Airfoil. In *CFD Society of Canada*. Canmore, Alberta.

Leontini, J. S., Thompson, M. C., & Hourigan, K. (2006). The beginning of branching behaviour of vortex-induced vibration during two-dimensional flow. *Journal of Fluids and Structures*, *22*, 857–864.

McKinney, W., & DeLaurier, J. (1980). The Wingmill: An Oscillating-Wing Windmill. *Journal of Energy*, *5*, 109–115.

Mendes, F., Poirel, D., & Benaissa, A. (2011). Experimental Investigation of Self-Sustained Pitch-Heave Aeroelastic Oscillations of a NACA0012 Airfoil at Transitional Reynolds Numbers. In *CASI2011*. Montreal, Canada.

Morissette, J. (2009). *Simulations aéroélastiques dailes oscillantes multi-segments par méthode vortex*. Master's thesis Université Laval.

Olivier, M. (2014). *A Fluid-Structure Interaction Partitioned Algorithm Applied to Flexible Flapping Wing Propulsion*. Ph.D. thesis Laval University. URL: http://www.theses.ulaval.ca/2014/30609/).

OpenCFD (2012a). *OpenFOAM - The Open Source CFD Toolbox - Programmer's Guide*. OpenCFD Ltd. United Kingdom. Version 2.1.1.

OpenCFD (2012b). *OpenFOAM - The Open Source CFD Toolbox - User's Guide*. OpenCFD Ltd. United Kingdom. Version 2.1.1.

Peng, Z., & Zhu, Q. (2009). Energy harvesting through flow-induced oscillations of a foil. *Physics of Fluids*, *21*, 1–9.

Poirel, D. (2012). private communication.

Poirel, D., Harris, Y., & Benaissa, A. (2006). Aeroelastic dynamics of a NACA 0012 airfoil in the transitional Reynolds number regime. In *2006 Summer Conference of the ASME Pressure Vessels and Piping Division*. Vancouver, Canada. Paper PVP2006-ICPVT11-93957.

Poirel, D., Harris, Y., & Benaissa, A. (2008). Self-sustained aeroelastic oscillations of a NACA0012 airfoil at low-to-moderate Reynolds numbers. *Journal of Fluids and Structures*, *24*, 700–719.

Poirel, D., & Mendes, F. (2011). Experimental Investigation of Small Amplitude Self-Sustained Pitch-Heave Oscillations of a NACA0012 Airfoil at Transitional Reynolds Numbers. In *50th AIAA Aerospace and Science Meeting*. Nashville, Tennessee.

Razak, N. A., Andrianne, T., & Dimitriadis, G. (2011). Flutter and stall flutter of a rectangular wing in a wind tunnel. *AIAA Journal*, *49*, 2258–2271.

Rumsey, C. L., & Spalart, P. R. (2008). Turbulence model behavior in low reynolds number regions of aerodynamic flowfields. In *38th AIAA Fluid Dynamics Conference and Exhibit*. Seattle, Washington.

Shimizu, E., Isogai, K., & Obayashi, S. (2008). Multiobjective design study of a flapping wing power generator. *Journal of Fluids Engineering*, *130*, 1–8.

Spalart, P. R. (2000). Trends in turbulence treatments. In *AIAA Fluids 2000 Conference and Exhibit*. Denver, Colorado.

Spalart, P. R., & Allmaras, S. R. (1994). One-equation turbulence model for aerodynamic flows. *La Recherche Arospatiale*, (pp. 5–21).

Spalart, P. R., & Rumsey, C. L. (2007). Effective inflow conditions for turbulence models in aerodynamic calculations. *AIAA Journal*, *45*, 2544–2553.

Tan, Y. K. (2011). *Suistainable Energy Harvesting Technologies - Past, Present and Future*. InTech. doi:10.5772/945.

Tezduyar, T., Sathe, S., Keedy, R., & Stein, K. (2006). Space-time finite element techniques for computation of fluid-structure interactions. *Computer Methods in Applied Mechanics and Engineering*, *195*, 2002–2027.

Tian, F. (2014). Fsi modeling with the dsd/sst method for the fluid and finite difference method for the structure. *Computational Methods*, *54*, 581–589.

Tian, F., Dai, H., Luo, H., Doyle, J., & Rousseau, B. (2014). Fluid-structure interaction involving large deformations: 3d simulations and applications to biological systems. *Journal of Computational Physics*, *258*, 451–469.

Veilleux, J.-C. (2014). Numerical study of self-sustained pitch-heave oscillations of an elastically supported airfoil. Master's thesis, Dept. of Mechanical Engineering, Laval University, Quebec, Canada; http://www.theses.ulaval.ca/2014/31139/.

Wildi, T., & Sybille, G. (2000). *Electrotechnique*. (3rd ed.). Qubec, Canada: Les Presses de l'Universit Laval.
Williamson, C. H. K., & Govardhan, R. (2004). Vortex-induced vibrations. *Annual Review of Fluid Mechanics*, *36*, 413–455.
Wu, B., Lang, Y., Zargari, N., & Kouro, S. (2011). *Power Conversion and Control of Wind Energy Systems*. Hoboken, New Jersey: Wiley.
Xiao, Q., & Zhu, Q. (2014). A review on flow energy harvesters based on flapping foils. *Journal of Fluids and Structures*, *46*, 174–191.
Yang, J., Preidikman, S., & Balaras, E. (2008). A strongly coupled, embedded-boundary method for fluid-structure interactions of elastically mounted rigid bodies. *Journal of Fluids and Structures*, *24*, 167–182.
Young, J., Lai, J. C. S., & Platzer, M. F. (2014). A review of progress and challenges in flapping foil power generation. *Progress in Aerospace Sciences*, *67*, 1–28. doi:10.1016/j.paerosci.2013.11.001.
Zhu, Q. (2011). Optimal frequency for flow energy harvesting of a flapping foil. *Journal of Fluid Mechanics*, *675*, 495–517.
Zhu, Q., Haase, M., & Wu, C. H. (2009). Modeling the capacity of a novel flow-energy harvester. *Applied Mathematical Modelling*, *33*, 2207–2217.
Zhu, Q., & Peng, Z. (2009). Mode coupling and flow energy harvesting by a flapping foil. *Physics of Fluids*, *21*.